

A conceptual Investigation of Turbidity Current Trigger from Alongshelf Current-supported Turbidity Currents

Celalettin Emre Ozdemir¹, Liangyi Yue², Haq Murad Nazari³, Z. George Xue⁴, Samuel J. Bentley³, Shuo Yang⁵, Sayed O Hofioni³, Robert Forney³, and Saber Aradpour³

¹Civil and Environmental Engineering, Louisiana State University

²Stanford University

³Louisiana State University

⁴LSU

⁵Louisiana State University

December 7, 2022

Abstract

Wave- and current-supported turbidity currents (WCSTCs) are one of the sediment delivery mechanisms from the inner shelf to the shelf break. Therefore, they play a significant role in the global cycles of geo-chemically important particulate matter. Recent observations suggest that WCSTCs can transform into self-driven turbidity currents close to the continental margin. However, little is known regarding the critical conditions that grow self-driven turbidity currents on WCSTCs. This is in part due to the knowledge gaps in the dynamics of WCSTCs regarding the role of density stratification. Especially the effect of sediment entrainment, and the parameters thereof, on density stratification and the amount of sediment suspension, has been overlooked. To this end, this study revisits the existing theoretical framework for a simplified WCSTC, in which waves are absent, i.e., alongshelf current-supported turbidity current (ACSTC). A depth-integrated advection model is developed for suspended sediment concentration. The analyses of the model, which are verified by turbulence-resolving simulations, indicate that the amount of suspended sediment load is regulated by the equilibrium among density stratification, positive feedback between entrainment and cross-shelf gravity force, and settling flux dissociated with density stratification. It is also found that critical density stratification is not a necessary condition for equilibrium. A quantitative relation is developed for the critical conditions for self-driven turbidity currents, which is a function of bed shear stress, entrainment parameters, bed slope, and sediment settling velocity. In addition, the suspended sediment load is analytically estimated from the model developed.

1 **A conceptual Investigation of Turbidity Current**
2 **Trigger from Alongshelf Current-supported Turbidity**
3 **Currents**

4 **Celalettin E. Ozdemir^{1,2,3*}**

5 **Liangyi Yue⁴**

6 **Haq Murad Nazari¹**

7 **George Xue^{2,3,5}**

8 **Samuel J. Bentley^{3,6}**

9 **Shuo Yang¹**

10 **Sayed O. Hofioni¹**

11 **Robert Forney⁵**

12 **Saber Aradpour¹**

13 ¹Civil and Environmental Engineering, Louisiana State University, Baton Rouge LA 70803

14 ²Center for Computation and Technology, Louisiana State University, Baton Rouge LA 70803

15 ³Coastal Studies Institute, Louisiana State University, Baton Rouge LA 70803

16 ⁴Civil and Environmental Engineering, Stanford University, Stanford CA 94305

17 ⁵Department of Oceanography and Coastal Sciences, Louisiana State University, Baton Rouge LA 70803

18 ⁶Department of Geology and Geophysics, Louisiana State University, Baton Rouge LA 70803

*3240L Patrick Taylor Hall, Civil and Environmental Engineering, Louisiana State University, Baton Rouge LA 70803

19

Key Points:

20

• A time-dependent depth-integrated advection model for suspended sediment concentration is developed for ACSTCs.

21

22

• Parametric limits that delineate along-shelf current-supported turbidity currents from self-driven turbidity currents are quantified.

23

24

• Settling flux, stratification, and the nonlinear interaction between entrainment and cross-shelf gravity force govern the suspension amount.

25

Corresponding author: Celalettin E. Ozdemir, cozdemir@lsu.edu

Abstract

Wave- and current-supported turbidity currents (WCSTCs) are one of the sediment delivery mechanisms from the inner shelf to the shelf break. Therefore, they play a significant role in the global cycles of geo-chemically important particulate matter. Recent observations suggest that WCSTCs can transform into self-driven turbidity currents close to the continental margin. However, little is known regarding the critical conditions that grow self-driven turbidity currents on WCSTCs. This is in part due to the knowledge gaps in the dynamics of WCSTCs regarding the role of density stratification. Especially the effect of sediment entrainment, and the parameters thereof, on density stratification and the amount of sediment suspension, has been overlooked. To this end, this study revisits the existing theoretical framework for a simplified WCSTC, in which waves are absent, i.e., alongshelf current-supported turbidity current (ACSTC). A depth-integrated advection model is developed for suspended sediment concentration. The analyses of the model, which are verified by turbulence-resolving simulations, indicate that the amount of suspended sediment load is regulated by the equilibrium among density stratification, positive feedback between entrainment and cross-shelf gravity force, and settling flux dissociated with density stratification. It is also found that critical density stratification is not a necessary condition for equilibrium. A quantitative relation is developed for the critical conditions for self-driven turbidity currents, which is a function of bed shear stress, entrainment parameters, bed slope, and sediment settling velocity. In addition, the suspended sediment load is analytically estimated from the model developed.

Plain Language Summary

Turbidity currents are responsible for the rapid displacement of sediments to the deep ocean. Their triggering mechanisms can be numerous, but recent observations suggest that some of the turbidity currents originate from slowly moving turbidities driven by currents and waves, also known as wave- and current-supported turbidity currents. To identify the parametric limits of the transition mentioned, the existing theoretical frame-

53 work for slowly moving turbidity currents is re-appraised, and the amount of sediments
54 that can be carried by currents parallel to the shore is analytically evaluated. A para-
55 metric limit for the occurrence of fast-moving self-driven turbidity currents is developed.

56 **1 Introduction**

57 **1.1 Motivation**

58 Transport of river-borne sediments across the continental shelves to the continen-
59 tal margin is key to sediment source-to-sink and thus the global cycles of geochemically
60 important particulate matter. Wave- and current-driven sediment transport across the
61 shelves, known as wave- and current-supported turbidity currents (WCSTCs), are one
62 of the sediment-routing processes. The studies in the last three decades suggest that WC-
63 STCs are/were ubiquitous in modern/ancient oceans (Bhattacharya et al., 2016; Denom-
64 mee et al., 2016; Fain et al., 2007; Hale & Ogston, 2015; Jaramillo et al., 2009; Ma et
65 al., 2008, 2010; Macquaker et al., 2010; Martin et al., 2008; Ogston et al., 2008; Traykovski
66 et al., 2000, 2007, 2015; Walsh et al., 2004; Zang et al., 2020; Zhang et al., 2016; Peng
67 et al., 2022; Ayranci et al., 2012).

68 Recent studies provide evidence to that these slowly moving sediment suspensions
69 can trigger self-driven turbidity currents toward the shelf break (Ma et al., 2008; Sequeiros
70 et al., 2019), which swiftly transport sediments to the deep ocean. Especially, the anal-
71 ysis of turbidity currents over the Malaylay Canyon in the Phillippines between 2006 and
72 2016 (Sequeiros et al., 2019) suggests that sediments suspended in the shallow parts of
73 the Malaylay Bay (~ 15 m) slowly move toward the shelf break and transition to a self-
74 driven turbidity current. Similarly, observations on the Waipou Shelf in New Zealand
75 showed that wave- and current-driven sediment suspension thickened towards the shelf
76 break (Ma et al., 2008), again suggesting a trigger of a turbidity current from slowly mov-
77 ing WCSTCs. However, little is known as to the critical conditions that transform WC-

78 STCs to self-driven turbidity currents. To this end, there is a need to identify the phys-
79 ical processes that stabilize and destabilize WCSTCs and the parameters thereof.

80 The slow motion of WCSTCs across the continental shelf, thus their long sustenance
81 in time, suggests an equilibrium. The aforementioned equilibrium is the key assumption
82 of the existing conceptual framework for WCSTCs (Wright et al., 2001), which was rig-
83 orously analyzed and verified recently in Flores et al. (2018). The equilibrium mentioned
84 requires a steady velocity and concentration, which thus requires a balance between downs-
85 lobe gravity force and the opposing shear force at the bed. Acceleration of the cross-shelf
86 turbidity current is the natural indicator of a slow-moving WCSTC to rapid self-driven
87 turbidity current. This acceleration is possible when downslope gravity force exceeds the
88 friction force due potentially to sharpening shelf slope, sediment entrainment in excess
89 of deposition, or both. Conceivably, all these conditions lead to nonlinear growth of ve-
90 locity and concentration. For example, sediment entrainment in excess of deposition aug-
91 ments the cross-shelf gravity force and augmented cross-shelf gravity force leads to fur-
92 ther sediment entrainment from the bed. As will be discussed in detail throughout, sediment-
93 induced density stratification works against the described positive feedback loop as an
94 equilibrium-restoring agent. Sediment-induced density stratification is also nonlinear be-
95 cause of its dissipative effect on turbulence, which thus reduces sediment suspension (see
96 the review in Winterwerp (2001) and the references therein). Therefore, the critical con-
97 ditions for the trigger of self-driven turbidity current must be based on the quantifica-
98 tion of the competition between these two nonlinear processes, namely the positive feed-
99 back loop between sediment entrainment and the downslope gravity force as well as the
100 sediment-induced density stratification.

101 Yet, as will be discussed in the following subsection, the nonlinear processes can-
102 not be implemented into the existing models for WCSTCs. To this end, we will first sum-
103 marize the available conceptual framework for WCSTCs in Section 1.2 and critically re-
104 view this framework in Section 1.3 in light of the studies that followed in the literature.

105 Section 1.3 also summarizes the specific objectives and the hypotheses behind the ob-
 106 jectives.

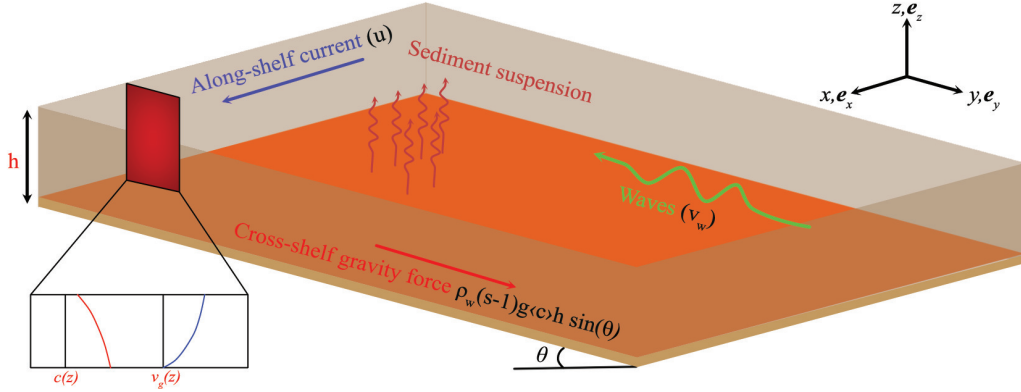


Figure 1: Descriptive sketch of WCSTCs. In the three-dimensional Cartesian coordinate system, x -, y -, and z -directions refer to the along-shelf, cross-shelf, and vertical directions, respectively. e_x , e_y , and e_z are the unit vectors in x -, y -, and z -directions. Along-shelf current, indicated by the blue arrow, with velocity u and shore-normal waves, indicated by undulated green arrow, with a root-mean-square wave velocity of v_w suspend sediment from the bed, which is indicated by undulated red arrows. The concentration profile of the sediment suspension is plotted in red illustrated on the panel at the bottom left corner. Sediment suspension creates a downslope gravity force of $(\rho_s - \rho_w)g\langle c \rangle h \sin \theta$, which also creates a downslope motion, whose velocity profile is shown in blue curve on the panel in the lower left corner.

107 **1.2 Wright et al. (2001)'s Conceptual Framework**

108 The peculiar characteristic of WCSTCs, which makes WCSTCs different from self-
 109 driven turbidity currents, is their requirement of wave and current boundary layer tur-
 110 bulence for their sustenance. In other words, sediments are kept in suspension with the
 111 aid of turbulence; if turbulence is removed, suspended sediments will deposit because the
 112 slow cross-shelf motion cannot sustain itself. Due to the equilibrium mentioned in Sec-
 113 tion 1.1, there is a balance between the cross-shelf gravity force and the friction force at
 114 the bed, which is formulated as

$$(s - 1)g\langle c \rangle h \sin \theta = C_d v_g \sqrt{v_g^2 + v_w^2 + u^2}, \quad (1)$$

115 where s is the specific gravity of suspended sediments, g is the gravitational accel-
 116 eration, h is the thickness of the turbidity, θ is the angle of cross-shelf bed slope, C_d is

117 the drag coefficient, v_g is the cross-shelf velocity of WCSTC, v_w is the wave velocity, and
 118 u is the alongshelf current velocity. Note that Equation 1 is cast by using the reference
 119 coordinate system in Figure 1. Volumetric sediment concentration is denoted as c , and
 120 the concentration used in Equation 1 is the depth-averaged concentration, where depth-
 121 averaged quantities are denoted as angled brackets. For the drag coefficient, $C_d \approx 0.003$ –
 122 0.006 was proposed as a proper range of drag coefficient by referring to Komar (1977)
 123 and van Kessel & Kranenburg (1996).

124 Wright et al. (2001) also suggested that depth-averaged concentration is controlled
 125 by the density stratification, which is quantified by the bulk Richardson number

$$\text{Ri}_b = \frac{(s-1)g\langle c \rangle h}{v_g^2 + v_w^2 + u^2}. \quad (2)$$

126 Bulk Richardson number was argued to be a close approximation of gradient Richard-
 127 son number, where concentration gradient is approximated to $\partial c / \partial z \approx \langle c \rangle / h$, and the
 128 square of the velocity gradient is approximated to $(\partial v / \partial z)^2 \approx (v_g^2 + v_w^2 + u^2) / h^2$. It
 129 was proposed that sediment suspension in WCSTCs must be critically stratified, and the
 130 bulk Richardson number must be $\text{Ri}_b = 0.25$ for critical density stratification. If strat-
 131 ification is weaker than critical density stratification ($\text{Ri}_b < 0.25$), sediment deficit will
 132 be compensated by sediment entrainment. If stratification is stronger than the critical
 133 stratification ($\text{Ri}_b > 0.25$), the excess suspension will deposit. For known v_g , v_w , and
 134 u , the suspended sediment load can be determined conveniently by imposing $\text{Ri}_b = 0.25$.

135 By combining Equations 1 and 2, imposing $v_g \gg u_w, v$ for self-supporting tur-
 136 bidity current, assuming $C_d = 0.003$ as the proper drag coefficient value, and using $\text{Ri}_b =$
 137 0.25 as the critical value for density stratification, Wright et al. (2001) obtained the crit-
 138 ical slope to maintain a self-supporting turbidity current as $\sin \theta = C_d / \text{Ri}_b = 0.003 / 0.25 =$
 139 0.012 .

1.3 Objectives

The described conceptual framework is only applicable to steady-state conditions because equilibrium is strictly enforced. The fact that there is no term associated with the sediment concentration's time rate of change—which would quantify the growth or decay in time—disallows WCSTC's growth into self-driven turbidity current. Equilibrium is enforced by imposing density stratification as the sole governing agent of sediment entrainment and deposition. This imposition ignores the potential role of fine sediment entrainment relations, which is well-established in the literature (see Sanford & Maa (2001) for an in-depth review). Quantifying sediment entrainment through density stratification cannot capture the positive feedback loop between sediment entrainment and downslope gravity force, which potentially triggers self-driven turbidity currents. This makes it impossible to calculate the triggering conditions from the available conceptual framework. It must be noted that the critical slope of 0.012 in Wright et al. (2001) is not the critical slope that triggers turbidity current but the minimum slope to maintain a self-supported turbidity current. This is because the trigger refers to the initiation of a rapidly moving transient turbidity current; whereas the self-supporting turbidity current is the self-driven turbidity current that forms after the aforementioned transient turbidity current reaches a steady state.

The disagreement in bulk Richardson numbers reported in the literature can perhaps be explained by the role of sediment entrainment parameters on the total suspended sediment load. Recent field observations close to the Rhine River mouth (Flores et al., 2018), numerical simulations for wave-supported turbidity currents (Yue et al., 2020), wave boundary layers (Cheng et al., 2015), alongshelf current supported turbidity currents (Haddadian et al., 2021), and laboratory experiments in oscillating water tunnel (Hooshmand et al., 2015) reported Ri_b as low as 0.01. To explain the reported discrepancy in Ri_b different arguments can be made. One can ascribe this discrepancy to winnowing (Parsons et al., 2007; Flores et al., 2018). For field and laboratory studies, win-

167 nowing can perhaps be a plausible but unproven explanation. However, numerical ex-
168 periments (Yue et al., 2020; Cheng et al., 2015; Haddadian et al., 2021) were conducted
169 for uniform sediment size; therefore, winnowing is not a valid explanation for low Ri_b in
170 numerical simulations.

171 In this study, a dynamic (time-dependent) depth-integrated concentration model
172 is developed. The model developed accounts for sediment entrainment from and depo-
173 sition to the bed as well as the density stratification. Non-linearities associated with the
174 positive feedback loop between the sediment entrainment and the downslope gravity force
175 as well as the density stratification are analytically approximated and incorporated into
176 the model. This model is used to determine the trigger conditions of self-driven turbid-
177 ity current that grows out of alongshelf current-supported turbidity currents (ACSTCs)
178 and the amount of total suspended sediment load in ACSTCs. The motivation behind
179 developing this model is to test the following hypotheses. First, *the total suspended sed-*
180 *iment load is regulated by the equilibrium among sediment entrainment, deposition, and*
181 *the density stratification created by the sediment suspension.* Second, because sediment
182 deposition is governed mainly by settling velocity, and the sediment entrainment is gov-
183 erned by the erosion parameters, *both the total suspended sediment amount and the crit-*
184 *ical conditions for the self-driven turbidity current trigger are functions of settling ve-*
185 *locity, entrainment parameters, and the parameters that quantify density stratification.*
186 Testing these hypotheses will therefore test the validity of whether the critical density
187 stratification is a required condition in ACSTCs.

188 The reason behind choosing ACSTCs in this study is twofold. First, toward the
189 shelf break waves lose intensity or vanish because of the increasing depth, making along-
190 shelf currents the dominant, perhaps the only, hydrodynamic driver. Second, ACSTCs
191 have relatively simpler hydrodynamics. In the presence of waves, nonlinear interactions
192 among waves, alongshelf currents, and cross-shelf propagation of the turbidity current
193 will make the problem more complicated, making it hard to draw conclusions as to the

194 role of density stratification. For example, the augmented drag coefficient when waves
 195 and the cross-shelf propagation aligns (Yue et al., 2020) is a result of the nonlinearity
 196 mentioned. In this regard, a systematic reductive approach —starting with a simplified
 197 case that will step-by-step include further complexities— will be more appropriate to un-
 198 derstand the respective role of each mechanism in WCSTCs.

199 The rest of the paper is structured as follows. In Section 2, numerical methods and
 200 the terminology will be described. Section 3 will present the overall results. In Section
 201 4, the development of a depth-integrated suspended sediment concentration model will
 202 be described, and the validation of the model against the simulation results will be pre-
 203 sented. Section 5 will summarize the findings with discussions.

204 **2 Methods**

205 **2.1 Problem Setup and Governing Equations**

206 Direct numerical simulations (DNSs) are conducted over a smooth channel with
 207 a mild spanwise slope, in which sediment entrainment is allowed at the bottom bound-
 208 ary. The spanwise slope creates a gravity force similar to those that drive the cross-shelf
 209 propagation of ACSTCs. Sediment velocity (\mathbf{u}^s) is obtained after the vectorial sum of
 210 the fluid (seawater) velocity (\mathbf{u}^f) and the settling velocity of sediments (w_s):

$$\mathbf{u}^s = \mathbf{u}^f + w_s \mathbf{e}_g, \quad (3)$$

211 where \mathbf{e}_g is the unit vector in the gravitational direction with respect to the bed,
 212 that is $\mathbf{e}_g = (0, \sin \theta \mathbf{e}_y, -\cos \theta \mathbf{e}_z)$ with \mathbf{e}_x , \mathbf{e}_y , and \mathbf{e}_z being the unit vectors point-
 213 ing in the along-shelf, cross-shelf, and the bed-normal directions, respectively (see Fig-
 214 ure 1). Sediment settling velocity is calculated as

$$w_s = \frac{(s-1)gd^2}{18\nu^f}, \quad (4)$$

215 following the Stokes law, which is valid for fine spherical sediments. In Equation 4,
 216 d is the sediment diameter and ν^f is the kinematic viscosity of the seawater. The diam-
 217 eter range of sediments used in the simulations ($d = [6 \times 10^{-6}, 20 \times 10^{-6}]$ m) is suffi-
 218 ciently small to use the Stokes Law for the sediment settling velocity.

219 As it will be shown in Section 3.2, sediment concentration does not exceed 2 kg m^{-3} ,
 220 suggesting that sediment suspension is dilute. Dilute sediment suspension allows us to
 221 impose the continuity equation for the seawater:

$$\nabla \cdot \mathbf{u}^f = 0. \quad (5)$$

222 The momentum equation of the seawater is given as

$$\frac{\partial \mathbf{u}^f}{\partial t} + \mathbf{u}^f \cdot \nabla \mathbf{u}^f = \frac{u_{\tau_o}^2}{h} \mathbf{e}_x + \frac{1}{\rho} \nabla p' + (s-1)gc \mathbf{e}_g + \nu^f \nabla^2 \mathbf{u}^f. \quad (6)$$

223 Here, the friction velocity due to alongshelf current is denoted as $u_{\tau_o} = \sqrt{\tau_{bo}/\rho^f}$,
 224 where τ_{bo} and ρ^f are the bed shear stress due to alongshelf current and the density of
 225 the seawater, respectively. The alongshelf current is driven by a uniform pressure gra-
 226 dient equal to $u_{\tau_o}^2/h$, where h is the flow depth and is the first term on the right-hand
 227 side of Equation 6. When integrated along the bed-normal direction, this term will counter
 228 the bed shear stress created by the along-shelf current normalized by the density of the
 229 seawater per unit mass, that is τ_{bo}/ρ^f . The second term on the right-hand side will both
 230 force the cross-shelf flow through $(s-1)gc \sin \theta \mathbf{e}_y$ and accounts for the density strat-
 231 ification due to vertical buoyancy force $-(s-1)gc \cos \theta \mathbf{e}_z$.

232 The governing equation for the suspended sediment concentration is the advection-
 233 diffusion equation, valid for fine sediment suspension (Cantero et al., 2008). The advection-
 234 diffusion equation is given as

$$\frac{\partial c}{\partial t} + \mathbf{u}^s \cdot \nabla c = \mathcal{D} \nabla^2 c, \quad (7)$$

235 where \mathcal{D} is the effective diffusivity of the sediment concentration, which is selected
 236 to be equal to the kinematic viscosity of the seawater.

237 **2.2 Computational Domain and Boundary Conditions**

238 The governing equations are solved for a planar computational domain. The size
 239 of the domain in x -, y -, and z -directions is $4\pi h \times 2\pi h \times h$. The number of grid points
 240 in the corresponding directions is $256 \times 128 \times 257$. The selected domain size is suffi-
 241 cient to capture the largest eddies, and the resolution is sufficient to resolve the small-
 242 est eddy size formed. A detailed discussion regarding the domain size selection will fol-
 243 low in Section 2.3.

244 Periodic boundary conditions in x - and y -directions are specified for concentra-
 245 tion and velocity. Given that the equilibrium conditions are established in ACSTCs, choos-
 246 ing periodic boundary conditions in x - and y -directions is proper. At the bed, a no-
 247 slip boundary condition is imposed for the fluid velocity. The top boundary for the fluid
 248 phase is defined as a rigid lid, wherein the fluid can slip in x - and y -directions, but the
 249 vertical motion is not allowed, that is $\partial u^f / \partial z = \partial v^f / \partial z = 0$, and $w^f = 0$ at $z = h$.

250 The bottom boundary condition for sediment entrainment is specified following the
 251 previous studies (Cheng et al., 2015; Yue et al., 2020; Haddadian et al., 2021):

$$-\mathcal{D} \frac{\partial c}{\partial z} - w_s c \Big|_{z=0} = \mathcal{E} - \mathcal{D}, \quad (8)$$

252 where \mathcal{E} and \mathcal{D} respectively refer to the erosion and deposition fluxes. For the ero-
 253 sion flux, Partheniades-Arthurai-type formulation is adopted (Sanford & Maa, 2001)

$$\mathcal{E} = \begin{cases} m_e \left(\frac{\|\tau_b \cdot \mathbf{s}\|}{\tau_c} - 1 \right), & \text{if } \|\tau_b\| > \tau_c \\ 0, & \text{if } \|\tau_b\| < \tau_c \end{cases}, \quad (9)$$

254 where m_e is the erosion rate, and τ_c is the critical shear stress for erosion. $\|\tau_b \cdot \mathbf{s}\|$
 255 is the magnitude of the tractive (or shear) force over a unit area with \mathbf{s} being the unit
 256 vector pointing in the shear force direction at the bed. Magnitude-wise, bed shear stress
 257 and the shear force over a unit area are the same. Because shear stress is a tensor, it has
 258 to be vectorized to account for the along- and cross-shelf shear force components, lead-
 259 ing to the notation in Equation 9 and the equations that follow. The deposition flux is
 260 calculated as

$$\mathcal{D} = w_s c \Big|_{z=0}. \quad (10)$$

261 **2.3 Parameter Selection**

262 As it will be clearer in Section 3, the analytical model developed for the depth-integrated
 263 concentration is significantly affected by the sediment-induced density stratification. There-
 264 fore, the scales associated with turbulence and density stratification must be resolved.
 265 Resolving the scales mentioned arguably requires using DNS. On the other hand, sim-
 266 ulating ACSTCs at a realistic scale by DNS is almost impossible due to computational
 267 requirements. To this end, a downscaled ACSTC, which will be referred to as miniature
 268 ACSTC (Haddadian et al., 2021), will be used. For the miniature ACSTC, the flow depth
 269 is selected as $h = 0.10$ m, the initial bed shear stress is $\tau_{bo} = 0.013$ Pa, the critical
 270 shear stress is selected as $\tau_c = 0.01$ Pa. The bed shear stress imposed corresponds to
 271 a friction velocity of $u_{\tau o} = 0.0036$ m s⁻¹. The importance of friction velocity arises
 272 because it scales the velocity profile, which affects the Reynolds number. For developed
 273 turbulence to occur, the Reynolds number must be sufficiently high so that scale change
 274 will minimally impact the turbulent features. With the imposed friction velocity, one can

275 obtain the Reynolds number as $Re = 7 \times 10^4$ (see Haddadian et al., 2021), where the
 276 Reynolds number is defined as

$$Re = \frac{\langle u \rangle h}{\nu f}. \quad (11)$$

277 In Equation 11, $\langle u \rangle$ is the depth-averaged along-shelf velocity.

278 Downscaling ACSTCs will especially require the idealization of the critical shear
 279 stress and the scales associated with sediment transport. Although the turbulent flow
 280 is developed, the bed shear stress, which is $\tau_{bo} = 0.013$ Pa, can only erode loose fine
 281 sediments at the bed (Curran et al., 2007). Increasing the bed shear stress, even slightly,
 282 will add significant computational expense due to the increasing Reynolds number. There-
 283 fore, we selected the critical bed shear stress as $\tau_c = 0.010$ Pa and the entrainment rate
 284 $m_e = 3.6 \times 10^{-7}$ m s⁻¹, which are close to what has been used in previous studies for
 285 wave boundary layers (Cheng et al., 2015; Yue et al., 2020) and ACSTCs (Haddadian
 286 et al., 2021).

287 As it will be described in Section 3.2, settling velocity is the key parameter to change
 288 the density stratification and the sediment mass exchange at the bed. Therefore, sed-
 289 iment settling velocity normalized by the friction velocity is varied from $w_s/u_{\tau_o} = 0.01$
 290 to $w_s/u_{\tau_o} = 0.1$ (see Table 1 for w_s/u_{τ_o} values used in each simulation). Because the
 291 nonlinearity associated with the sediment entrainment and the cross-shelf gravity force
 292 in part depends on the cross-shelf bed slope, that is $\sin \theta$, specifying two different val-
 293 ues for $\sin \theta$ will provide us with a wide range of cross-shelf gravity force to assess the
 294 nonlinearity mentioned.

295

Table 1: Simulated cases and input parameters.

Case	w_s/u_{τ_o}	$\sin \theta$	m_e/u_{τ_o}	τ_{bo}/τ_c
A1	0.10	0.01	1×10^{-4}	0.25
A2	0.08	0.01	1×10^{-4}	0.25
A3	0.06	0.01	1×10^{-4}	0.25
A4	0.04	0.01	1×10^{-4}	0.25
A5	0.02	0.01	1×10^{-4}	0.25
A6	0.01	0.01	1×10^{-4}	0.25
B1	0.10	0.005	1×10^{-4}	0.25
B2	0.08	0.005	1×10^{-4}	0.25
B3	0.06	0.005	1×10^{-4}	0.25
B4	0.04	0.005	1×10^{-4}	0.25

296 Although idealized, the simulations will guide the development of the depth-integrated
 297 concentration model and validate the model results. Especially, sediment turbulence in-
 298 teraction, significantly altering the suspended sediment load, is resolved through DNS.
 299 The fidelity of the simulations to capture the fluid-sediment interaction will be presented
 300 in Section 3.2.

301 2.4 Numerical Methods

302 The governing equations are integrated in time by a third-order low-storage Runge-
 303 Kutta scheme (Williamson, 1980) with a maximum Courant-Friedrichs-Lewy number of
 304 0.5. Applying the pseudospectral scheme following Cortese & Balachandar (1995), the
 305 carrier flow phase is numerically solved with the corresponding boundary conditions (Equa-
 306 tion 8). During each of the three time levels in a computational step, the standard two-
 307 stage (predictor and corrector) projection method (Chorin, 1968) is utilized to enforce
 308 a divergence-free velocity field of the carrier flow. Right after the velocity projection, that
 309 is Equation 7, the sediment volumetric concentration is computed by solving the advection-
 310 diffusion equation in a way similar to the predictor stage of carrier flow with the corre-
 311 sponding boundary conditions. For further details, the reader is referred to Yue et al.
 312 (2019).

313 **2.5 Notation and Terminology**

314 Because different averaging techniques will be used, defining the averaging tech-
 315 niques in this subsection will provide convenience to the reader. Mean velocity and con-
 316 centration, discerned by an overbar, are obtained after averaging them over each hor-
 317 izontal plane at every vertical point and the sampling time T :

$$\langle \bar{\cdot} \rangle = \frac{1}{L_x L_y T} \int_{t_o}^{t_o+T} \int_{y=0}^{y=L_y} \int_{x=0}^{x=L_x} (\cdot) dx dy dt, \quad (12)$$

318 where t_o is the initial time of equilibrium. Note that mean quantities vary in depth.
 319 Whether the flow reached equilibrium was identified as the instant when the time series
 320 of the depth-averaged quantities', such as velocity and Reynolds shear stress, moving av-
 321 erage becomes constant. The moving average is calculated over a period of 5.44 seconds.
 322 For reliable turbulence statistics, T is ensured to be long enough so that the averaged
 323 quantities become insensitive to increasing T . Depth-averaged quantities, indicated by
 324 angled brackets, are computed from

$$\langle \cdot \rangle = \frac{1}{h} \int_{z=0}^{z=h} (\cdot) dz. \quad (13)$$

326 **3 Results and Discussions**

327 **3.1 Overview**

328 The conducted simulations resulted in two unstable cases wherein the depth-averaged
 329 sediment concentration grew substantially, which is presented in Figure 2. The two cases
 330 mentioned correspond to the lowest settling velocity, namely $w_s/u_{\tau_o} = 0.01$ and 0.02
 331 for $\sin \theta = 0.01$. In these two cases, there is no sign of equilibrium, but instead, the con-
 332 centration started accelerating past a certain time step, which is 360 s and $t = 840$ s
 333 for $w_s/u_{\tau_o} = 0.01$ and 0.02 , respectively. It is concluded that a self-driven turbidity cur-
 334 rent formed, and the simulations were terminated shortly after those instants. The rea-

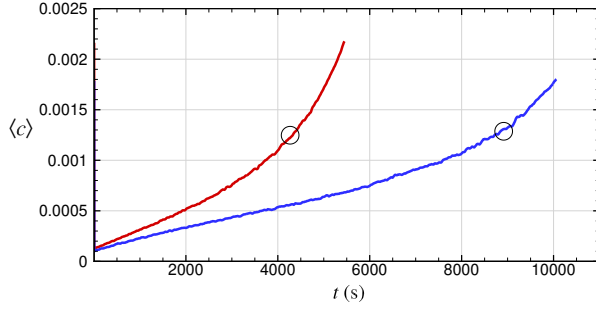


Figure 2: Time series of depth-averaged volumetric sediment concentration of the two unstable cases with $w_s/u_{\tau o} = 0.01$ and $w_s/u_{\tau o} = 0.02$ in which the cross-shelf slope is $\sin \theta = 0.01$. In both cases, suspended sediment concentration substantially grows without showing a sign of equilibrium, and the growth rate increases past a critical instance marked by a hollow circle, which is inferred from the time series of $\partial \langle c \rangle / \partial t$ (not shown).

335 son for termination is that the small domain size can only capture the very early stage
 336 of self-driven turbidity current growth. As sediments get finer, they can be easily sus-
 337 pended to elevations higher than the domain height. In the current setup, however, they
 338 are entrapped in a small domain due to no sediment outflux at the top. As such, sed-
 339 iment concentration will grow in a bounded domain, a physical situation irrelevant to
 340 the growth of self-driven turbidity currents after its very early stage. In this regard, the
 341 small domain for the miniature representation of ACSTCs is not sufficient to capture the
 342 whole process of self-driven turbidity current growth but its early stages. Indeed, these
 343 two simulations fall into the unstable region in the parametric space, that is, the region
 344 of ACSTCs' transition to self-driven turbidity currents, which will be discussed in de-
 345 tail in Section 4.3.1.

346 For stable cases, the time series of the bulk Richardson number is plotted in Fig-
 347 ure 3a instead of depth-averaged concentration. Doing so will serve to assess whether
 348 the bulk Richardson number reaches a global constant value, which was suggested in the
 349 previous studies (Wright et al., 2001; Wright & Friedrichs, 2006). Because conclusions
 350 from the Ri_b time series are similar for both slopes, Figure 3a plots Ri_b time series for
 351 only $\sin \theta = 0.01$ for brevity. Figure 3a suggests that Ri_b equilibrates at different val-
 352 ues for different sediment settling velocities, and its order of magnitude is almost a decade

353 smaller than 0.25. Another observation is that the bulk Richardson number gets larger
 354 with decreasing settling velocity. From the definition of Ri_b , one may conjecture that ve-
 355 locity and the density gradients may not be accurately captured in Ri_b to measure the
 356 density stratification. In Figure 3b, we, therefore, plot the gradient Richardson number
 357 profiles, which is a stronger measure of density stratification. The gradient Richardson
 358 number, Ri_g , is defined as

$$359 \quad Ri_g = -\frac{(s-1)g\frac{\partial \bar{c}}{\partial z}}{\left(\frac{\partial \bar{u}_g}{\partial z}\right)^2 + \left(\frac{\partial \bar{v}}{\partial z}\right)^2}. \quad (14)$$

360 Profiles of Ri_g from the simulations do not collapse onto a single curve. Especially
 361 outside the near-bed region, the values of Ri_g decrease with increasing settling velocity.
 362 The magnitude range of Ri_g is almost three times that of Ri_b , especially outside the near-
 363 bed region. Our first conclusion from the time series of Ri_b and profiles of Ri_g is that
 364 the bulk Richardson number does not adequately capture the sediment-induced density
 365 stratification because there is a significant mismatch between the magnitudes of Ri_g and
 366 Ri_b . Because the gradient Richardson number profiles differ in magnitude despite the
 367 equilibrium, our second conclusion is that critical density stratification does not occur
 368 in the current simulations. This strengthens our hypothesis on the regulatory role of sed-
 369 iment entrainment and deposition on the total suspended sediment load. In the follow-
 370 ing subsection, eddy diffusivity and suspended sediment concentration profiles will be
 371 presented and analyzed regarding the respective roles of density stratification and the
 372 sediment mass exchange at the bed.

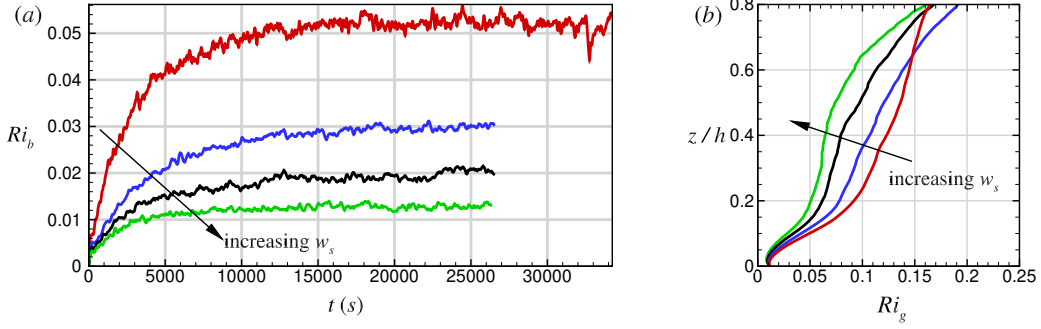


Figure 3: (a) Time series of bulk Richardson number for cases with $\sin \theta = 0.01$. The arrow indicates the reduction of Ri_b in magnitude with increasing w_s . Time series of Ri_b for $\sin \theta = 0.005$ also shows a similar trend and is therefore not shown for brevity. (b) Gradient Richardson number profiles for the same cases in panel (a). In both subfigures, red, blue, black, and green curves indicate $w_s/u_{\tau_o} = 0.04, 0.06, 0.08, \text{ and } 0.10$, respectively.

373

3.2 Concentration and Eddy Diffusivity Profiles

374

375

376

377

378

379

380

381

382

383

To facilitate an informed discussion on the role of sediment entrainment, deposition, and density stratification on the amount of suspended sediment concentration, let us momentarily ignore the effects of density stratification. In the absence of density stratification, the amount of sediment suspension depends on the sediment entrainment at the bed and the shape of the concentration profile, which are tightly linked to the settling velocity, w_s . The shape of the concentration profile is important because the rate of deposition will increase as the concentration profile is skewed towards the bed. The role of w_s on the shape of the concentration profile can be realized through the balance between the settling flux, $w_s \bar{c}(z)$, and the turbulent suspension $\overline{c'w'}$, which can also be quantified as $-\mathcal{D}_t \bar{c}/dz$:

$$-\mathcal{D}_t \frac{d\bar{c}}{dz} = w_s \bar{c}(z). \quad (15)$$

384

385

386

387

The concentration gradient, which can be considered as a proxy for the shape of the concentration profile, becomes $-w_s \bar{c}/\mathcal{D}_t$. This suggests that decreasing w_s or increasing \mathcal{D}_t makes the concentration profile's shape more uniform; whereas increasing w_s or decreasing \mathcal{D}_t skews the sediment concentration towards the bed. It is clear that sed-

388 iment settling velocity is one of the governing parameters of the concentration profile's
 389 shape, even in the absence of density stratification. Sediment settling velocity is also a
 390 governing parameter of sediment mass exchange at the bed, which can be realized af-
 391 ter rearranging the bottom boundary condition for sediment concentration at the bed,
 392 that is, $c_b = m_e/w_s(\bar{\tau}_b/\tau_c - 1)$.

393 It is worth noting that Equation 15 also provides us with the required resolution
 394 to quantify the density, or concentration, gradient, which is \mathcal{D}_t/w_s . The eddy diffusiv-
 395 ity varies with depth and approaches zero towards the bed. As such, there is a high res-
 396 olution requirement, especially near the bed, which cannot be captured by the bulk Richard-
 397 son number.

398 When density stratification is present, the role of settling velocity on the shape of
 399 the concentration profile becomes convoluted. This is because settling velocity is also
 400 a governing parameter of sediment-induced density stratification and the turbulence dis-
 401 sipation thereof (Winterwerp, 2001; Cantero et al., 2012; Winterwerp et al., 2009; Ozdemir
 402 et al., 2011; Haddadian et al., 2021). With turbulence is dissipated, sediment mixing re-
 403 duces, and so does the eddy diffusivity. The shape of the concentration profile, there-
 404 fore, changes in concert with the shape of the eddy diffusivity profile. In this regard, through-
 405 out this section, simulated concentration profiles are mostly presented in the context of
 406 their shape, the balance between deposition and sediment entrainment, and the govern-
 407 ing parameters thereof.

408 For informed interpretation, it is worth discussing the application of the Monin-
 409 Obukhov theory in stratified sediment-laden flows, on which we will construct our model.
 410 The eddy diffusivity and suspended sediment concentration profiles in stratified sediment-
 411 laden flows can be obtained by using the Monin-Obukhov theory (Monin & Obukhov,
 412 1954). From the Monin-Obukhov theory, the eddy diffusivity profile is obtained as

$$\mathcal{D}_t = \frac{u_{\tau o} \kappa z}{S_c} \left(\frac{1 - \frac{z}{h}}{1 + \alpha \frac{z}{\mathcal{L}}} \right), \quad (16)$$

413 where \mathcal{L} is the Monin-Obukhov length scale, and κ is the von Kármán constant.
 414 The Schmidt number, S_c , is the ratio between the eddy viscosity (ν_t) and the sediment
 415 diffusivity (\mathcal{D}_t), that is $S_c = \nu_t/\mathcal{D}_t$. α is an empirical coefficient, which was proposed
 416 to be 5 in (Monin & Obukhov, 1954). It is worth noting that the Monin-Obukhov length
 417 scale (\mathcal{L}) measures the turbulence production relative to the buoyancy dissipation. As
 418 such, increasing \mathcal{L}^{-1} suggests strengthening buoyancy dissipation relative to turbulence
 419 production (see Winterwerp et al., 2009; Haddadian et al., 2021, for further discussion).
 420 As was shown in Winterwerp et al. (2009) and Haddadian et al. (2021) the ratio between
 421 the depth (h) and the Monin-Obukhov length scale (\mathcal{L}), which will be denoted as the
 422 Monin-Obukhov parameter (\mathcal{M}) henceforth, can be expressed in terms of the settling
 423 velocity (w_s), friction velocity ($u_{\tau o}$), and the depth-averaged concentration ($\langle c \rangle$):

$$\mathcal{M} = \alpha \frac{h}{\mathcal{L}} = \alpha \frac{(s-1)g\langle c \rangle h}{u_{\tau o}^2} \frac{w_s}{u_{\tau o}}. \quad (17)$$

424 By using the Monin-Obukhov parameter, eddy diffusivity profile can also be ex-
 425 pressed as

$$\mathcal{D}_t = \frac{u_{\tau o} \kappa z}{S_c} \left(\frac{1 - \frac{z}{h}}{1 + \mathcal{M} \frac{z}{h}} \right). \quad (18)$$

426 From Equation 17 and Equation 18, it is clear that both increasing concentration
 427 and settling velocity dissipate eddy diffusivity and are the governing parameters of den-
 428 sity stratification. Eddy diffusivity profile in Equation 18 allows for an analytical solu-
 429 tion of the sediment concentration profile (Itakura & Kishi, 1980):

$$c = c_o \left(\frac{z}{z_o} \frac{h - z_o}{h - z} \right)^{-\mathcal{R}} \left(\frac{h - z_o}{h - z} \right)^{-\mathcal{R}\mathcal{M}}. \quad (19)$$

430 where z_o is the reference height, c_o is the reference concentration, and $\mathcal{R} = w_s / (S_c \kappa u_{\tau o})$
 431 is the Rouse number. Note that the definition of the Rouse number here includes the Schmidt
 432 number (S_c) to make the following equations concise. Without the last term on the right-
 433 hand side, the concentration profile becomes identical to the Rouse profile, which is

$$c = c_o \left(\frac{z}{z_o} \frac{h - z_o}{h - z} \right)^{-\mathcal{R}}. \quad (20)$$

434 The concentration profile in Equation 19 will therefore be referred to as the mod-
 435 ified Rouse profile henceforth.

436 The eddy diffusivity and concentration profiles obtained from the simulations are
 437 presented in Figure 4. In Figure 4a, the close match between the observed eddy diffu-
 438 sivity profiles from the simulations and those estimated by Equation 16 is obtained by
 439 treating α , the empirical coefficient in Monin-Obukhov's self-similarity function, as a free
 440 variable. α ranges between $\alpha = 3.8$ and $\alpha = 4.7$ (see Table 1), which is similar to those
 441 reported in Haddadian et al. (2021). It is worth mentioning that α approaches 5 with
 442 strengthening density stratification. This point deserves further investigation but not within
 443 the scope of this study. The Schmidt number S_c used to obtain the eddy diffusivity pro-
 444 files are the depth-averaged values of S_c between $z/h = 0.1$ and $z/h = 0.9$ because
 445 turbulence becomes prevalent in the range selected (see Figure 4b for the profiles of S_c).
 446 The range of Schmidt number is $S_c = [0.89, 1]$, which falls onto its suggested values (Cellino
 447 & Graf, 1999). Eddy diffusivity profiles are also compared with their parabolic counter-
 448 part that develops in non-stratified media (dashed black curve in Figure 4a). This com-
 449 parison suggests a reduction in the magnitude of the eddy diffusivity with decreasing set-
 450 tling velocity, which clearly indicates enhanced turbulence dissipation with decreasing
 451 settling velocity. This is mainly because sediment suspension increases with the reduc-

Table 2: Observed parameters from the simulations that reached equilibrium. Cases A5 and A6, which are excluded from the table, are the unstable cases; therefore, a quasi-steady depth-averaged concentration and velocity cannot be obtained.

Case	S_c	α	$\langle c \rangle \times 10^5$	\mathcal{M}	$\langle v_g \rangle$ (m s ⁻¹)	$\langle u \rangle$ (m s ⁻¹)	$\langle u_{max} \rangle$ (m s ⁻¹)	Ri_b
A1	0.89	4.00	4.04	2.02	2.9×10^{-3}	71.40×10^{-3}	71.50×10^{-3}	0.013
A2	0.90	4.10	6.83	2.80	5.4×10^{-3}	74.80×10^{-3}	75.00×10^{-3}	0.020
A3	1.00	4.10	12.40	3.81	10.3×10^{-3}	80.40×10^{-3}	81.00×10^{-3}	0.031
A4	1.00	4.40	29.14	6.41	27.4×10^{-3}	91.10×10^{-3}	95.10×10^{-3}	0.052
B1	0.89	0.89	4.04	1.97	1.4×10^{-3}	71.30×10^{-3}	71.30×10^{-3}	0.013
B2	0.92	0.92	6.67	2.53	2.8×10^{-3}	75.00×10^{-3}	75.00×10^{-3}	0.019
B3	1.00	1.00	12.31	3.69	5.2×10^{-3}	80.10×10^{-3}	80.20×10^{-3}	0.031
B4	1.00	1.00	25.68	5.90	12.0×10^{-3}	89.30×10^{-3}	90.10×10^{-3}	0.051

452 tion in the settling velocity, which will be discussed shortly in this section. The peak of
 453 the eddy diffusivity is lowered in height as density stratification intensifies.

454 The comparison of the modified Rouse profile with those obtained from the sim-
 455 ulations in Figure 4(b,c) suggests a good agreement, which serves as a validation for the
 456 numerical model's fidelity to resolve turbulence and density stratification. It is worth not-
 457 ing that the concentration profiles in Figure 4b are normalized by the bed concentration
 458 to assess its shape. The modified Rouse profiles were obtained by choosing the reference
 459 height as $z_o = 0.01$ m, above which turbulence becomes prevalent. The modified Rouse
 460 profiles bend towards zero in the upper half of the depth when compared with the Rouse
 461 profile (compare the dashed curve with the solid curves in Figure 4c), which is consis-
 462 tent with the reduction in the eddy diffusivity. Reduction in concentration in modified
 463 Rouse profiles suggests a decline in total suspended sediment load with density strat-
 464 ification. Referring to the definition of the Monin-Obukhov parameter (\mathcal{M}) in Equation 17,
 465 one can conclude that the shape of the concentration profile is affected by both the set-
 466 tling velocity and the amount of sediment suspension.

467 Another observation from Figure 4c is that near-bed sediment concentration in-
 468 creases with decreasing w_s . This observation is closely related to the role of w_s on sed-

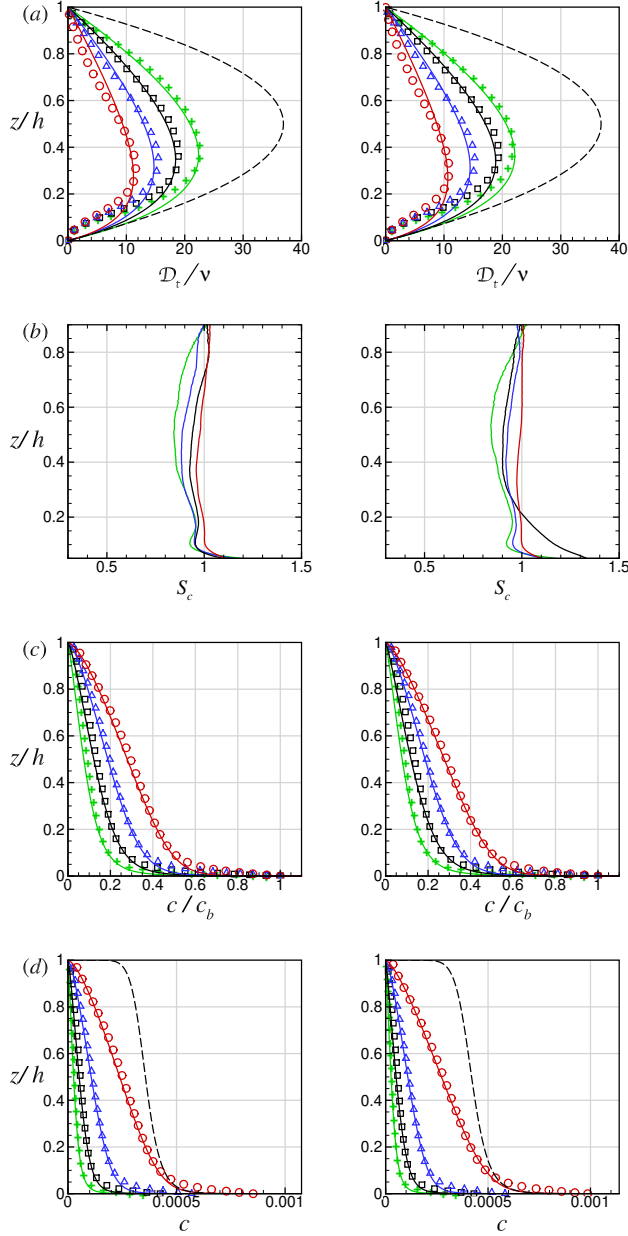


Figure 4: (a) Eddy diffusivity profiles normalized by the kinematic viscosity. (b) Schmidt number profiles. (c) Suspended sediment concentration profiles normalized by the concentration at the bed. (d) Volumetric suspended sediment concentration profiles. The first and the second rows plots the profiles of cases with $\sin \theta = 0.005$ and $\sin \theta = 0.01$, respectively. In all subfigures, red, blue, black, and green respectively identifies $w_s/u_{\tau_o} = 0.04, 0.06, 0.08$, and 0.10 . Solid curves on the left column indicate the eddy diffusivity estimated by the Monin-Obukhov theory (Equation 16), and the symbols of the same color as the curves indicate those obtained from the simulations. Solid curves on the second and the third columns estimate the modified Rouse profile from Equation 20, and symbols of the same color correspond to those obtained from the simulations. The dashed curves in (a) indicate the parabolic eddy diffusivity profile that occurs in unstratified media, and the dashed curves in (c) indicate the Rouse profile for $w_s/u_{\tau_o} = 0.04$ to emphasize the reduction in sediment concentration due to density stratification.

469 iment mass exchange at the bed. Noting that the critical shear stress for erosion is the
 470 same in all the simulations, near-bed concentration is inversely proportional to w_s , that
 471 is $\bar{c}_b \propto m_e/w_s(\bar{\tau}_b/\tau_c - 1)$.

472 The results presented in this section suggest that the total suspended load is gov-
 473 erned by sediment mass exchange at the bed and density stratification. The respective
 474 contributions of each mechanism to the total suspended load will be addressed by the
 475 dynamic depth-integrated concentration model, which will be discussed in the section
 476 that follows.

477 **4 Dynamic Depth-integrated Concentration Model**

478 To obtain the critical conditions for self-supported turbidity current trigger, a dy-
 479 namic (time-dependent) depth-integrated sediment concentration model is developed.
 480 Because equilibrium requires a statistically steady depth-integrated concentration, an
 481 equation that quantifies the depth-integrated concentration's variation in time will be
 482 a convenient tool to assess equilibrium. Upon integrating the advection-diffusion equa-
 483 tion for the sediment concentration and neglecting the diffusive term due to its negli-
 484 gible magnitude as opposed to the advective terms, we obtain the following equation

$$\frac{d\langle c \rangle h}{dt} = \frac{\partial \langle c \rangle h}{\partial t} + u^s \frac{\partial \langle c \rangle h}{\partial x} + v^s \frac{\partial \langle c \rangle h}{\partial y} = m_e \left(\frac{\|\tau_b \cdot \mathbf{s}\|}{\tau_c} - 1 \right) - w_s c_o. \quad (21)$$

485 The left-hand side of Equation 21 is the total derivative of the depth-integrated con-
 486 centration, that is $\langle c \rangle h$. The first and the second terms on the right-hand side respec-
 487 tively represent the sediment entrainment and settling fluxes at the bed, which are the
 488 source and sink terms, respectively. $\|\tau_b \cdot \mathbf{s}\|$ is the magnitude of the shear force at the
 489 bed over a unit area, which is the vector sum of those created in along- and cross-shelf
 490 directions. It must be noted that Equation 21 is dimensional, and all additive terms has
 491 a unit of m s^{-1} . Yet, keeping Equation 21 dimensional will make the equations that fol-
 492 low lengthy, creating inconvenience to the reader. Therefore, Equation 21 is nondimen-

493 sionalized by normalizing each term by u_{τ_o} , and expressing w_s/u_{τ_o} as $\kappa S_c \mathcal{R}$. In its non-
 494 dimensional form, Equation 21 reads

$$\frac{1}{u_{\tau_o}} \frac{d\langle c \rangle h}{dt} = \frac{m_e}{u_{\tau_o}} \left(\frac{\|\tau_b \cdot \mathbf{s}\|}{\tau_c} - 1 \right) - (\kappa S_c \mathcal{R}) c_o. \quad (22)$$

495 The dynamic depth-integrated concentration model will enable us to determine whether
 496 ACSTCs can remain in equilibrium or will grow to a self-driven turbidity current. For
 497 equilibrium, the right-hand side of Equation 22 must be zero. In other words, if erosion
 498 is countered by deposition, depth-integrated concentration will be in equilibrium; if not,
 499 there will be a growth in sediment suspension amount. The roles of density stratifica-
 500 tion and the positive feedback loop between the sediment suspension and sediment en-
 501 trainment are implicit in the erosion and deposition flux terms, respectively. As it will
 502 be shown in the following two subsections, these two mechanisms nonlinearly augment
 503 or reduce the suspended sediment amount. The following two subsections describe how
 504 nonlinearity in entrainment and deposition fluxes are obtained as explicit functions of
 505 $\langle c \rangle$.

506 4.1 Nonlinear Effect of Alongshelf Turbidity Currents on Entrainment

507 In the problem specified, the critical bed shear stress for erosion and bed shear stress
 508 due to along-shelf current are assumed to be known a priori. The augmented bed shear
 509 stress due to sediment suspension can simply be inferred from the bed shear stress, which
 510 is

$$\|\tau_b \cdot \mathbf{s}\| = \sqrt{\tau_{bo}^2 + [(s-1)g\langle c \rangle h \sin \theta]^2} \quad (23)$$

511 which is a function of the depth-averaged sediment concentration. To have a con-
 512 venient mathematical handle on the bed shear stress magnitude, we first rearrange Equa-
 513 tion 23 by normalizing it by τ_{bo} :

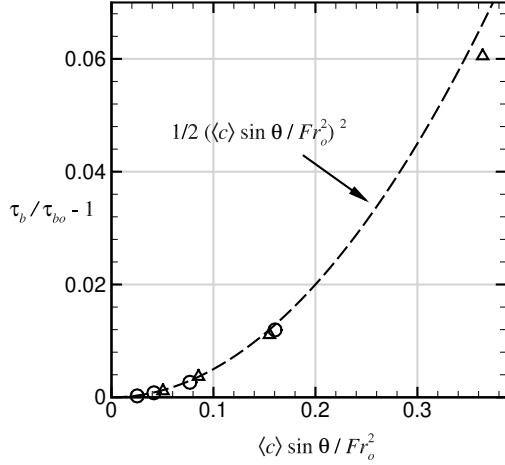


Figure 5: Variation of bed shear increase against the non-dimensional cross-shelf gravity force $\frac{\langle c \rangle}{Fr_o^2} \sin \theta$. The data shown is obtained from the simulations wherein hollow circles indicate the simulated results for $\sin \theta = 0.005$, and the hollow triangles indicate those for $\sin \theta = 0.01$.

$$\frac{\|\tau_b \cdot \mathbf{s}\|}{\tau_{bo}} = \sqrt{1 + \frac{[(s-1)g\langle c \rangle h \sin \theta]^2}{\tau_{bo}^2}}. \quad (24)$$

514 Equation 24 can further be simplified by defining a densimetric Froude number Fr_o

$$Fr_o = \frac{u_{\tau_o}}{\sqrt{(s-1)gh}}, \quad (25)$$

515 which will help express Equation 24 as

$$\frac{\|\tau_b \cdot \mathbf{s}\|}{\tau_{bo}} = \sqrt{1 + \left(\frac{\langle c \rangle \sin \theta}{Fr_o^2}\right)^2}. \quad (26)$$

516 As will be evident later in this section, expressing Equation 26 as a serial sum will
 517 help quantify the excess entrainment due to alongshelf current. The right-hand side of
 518 Equation 26 is therefore expanded as a binomial series sum:

$$\frac{\|\tau_b \cdot \mathbf{s}\|}{\tau_{bo}} = 1 + \frac{1}{2} \left(\frac{\langle c \rangle \sin \theta}{Fr_o^2} \right)^2 - \frac{1}{8} \left(\frac{\langle c \rangle \sin \theta}{Fr_o^2} \right)^4 + \frac{1}{16} \left(\frac{\langle c \rangle \sin \theta}{Fr_o^2} \right)^6 - \dots \quad (27)$$

519 Under equilibrium conditions or at the early stages of transition to self-driven tur-
 520 bidity currents, a weak nonlinearity is expected because of the dilute sediment concen-
 521 tration. The serial sum can hence be approximated to its first order:

$$\frac{\|\tau_b \cdot \mathbf{s}\|}{\tau_{bo}} \approx 1 + \frac{1}{2} \left(\frac{\langle c \rangle \sin \theta}{Fr_o^2} \right)^2. \quad (28)$$

522 Subtracting τ_{bo} from $\|\tau_b \cdot \mathbf{s}\|$ will isolate the bed shear stress increase, which is de-
 523 noted as $\Delta\tau_b$, as a function of the depth-integrated sediment concentration and is given
 524 as

$$\frac{\|\tau_b \cdot \mathbf{s}\| - \tau_{bo}}{\tau_{bo}} = \frac{\Delta\tau_b}{\tau_{bo}} = \frac{1}{2} \left(\frac{\langle c \rangle \sin \theta}{Fr_o^2} \right)^2. \quad (29)$$

525 This relation is compared with those obtained from the simulations in Figure 5.
 526 The estimated and observed values of $\Delta\tau_b$ agree well with a coefficient of determination
 527 of $r^2 = 0.996$, confirming the dilute suspended sediment assumption. The increase in
 528 the bed shear stress due to cross-shelf propagation of ACSTCs can therefore be isolated
 529 as

$$\frac{m_e}{u_{\tau o}} \left(\frac{\|\tau_b \cdot \mathbf{s}\|}{\tau_c} - 1 \right) = \frac{m_e}{u_{\tau o}} \left[\left(\frac{\tau_{bo}}{\tau_c} - 1 \right) + \frac{\Delta\tau_b}{\tau_c} \right]. \quad (30)$$

530 Denoting the normalized excess shear stress due to alongshelf current $\tau_{bo}/\tau_c - 1$
 531 as ξ and noting that $\Delta\tau_b/\tau_c = (\Delta\tau_b/\tau_{bo})(\tau_{bo}/\tau_c)$, Equation 30 can be expressed as an
 532 explicit function of $\langle c \rangle$ as follows:

$$\frac{m_e}{u_{\tau o}} \left(\frac{\|\tau_b \cdot \mathbf{s}\|}{\tau_c} - 1 \right) = \frac{m_e}{u_{\tau o}} \left[\xi + \left(\frac{1 + \xi}{2} \right) \left(\frac{\sin \theta}{Fr_o^2} \right)^2 \langle c \rangle^2 \right]. \quad (31)$$

533 Nonlinearity in sediment entrainment due to cross-shelf gravity force, which is the
 534 rightmost term within the brackets, is a quadratic function of the depth-averaged sus-
 535 pended sediment concentration. This term represents the positive feedback loop between
 536 the suspended sediment load and the bed shear stress magnitude. The nonlinearity men-
 537 tioned will be the main driver of the sediment suspension growth that will lead to self-
 538 driven turbidity currents.

539 4.2 Nonlinear Density Stratification Effect on Suspended Sediment Load

540 In Equation 22, the deposition flux is not an explicit function of $\langle c \rangle$ but expressed
 541 in terms of the bed concentration c_o . Therefore, we define a shape factor \mathcal{S} that links
 542 bed concentration to depth-averaged concentration:

$$\mathcal{S} = \frac{c_o}{\langle c \rangle}. \quad (32)$$

543 We term \mathcal{S} as the shape factor because it provides information as to the shape of
 544 the suspended sediment concentration profile (a similar definition for the shape factor
 545 is also given in Parker et al. (1986) for self-supporting turbidity currents). For example,
 546 \mathcal{S} becomes unity for uniform sediment concentration, whereas \mathcal{S} enlarges when concen-
 547 tration becomes skewed towards the bed. Strengthening density stratification will dampen
 548 eddy diffusivity, modulate the shape of the eddy diffusivity profile, and hence skew the
 549 concentration profile towards the bed. It follows that the shape factor must increase with
 550 strengthening stratification. In Section 3.2, density stratification is quantified by \mathcal{M} , and
 551 \mathcal{M} is a function of depth-averaged concentration and settling velocity (see Equation 17).
 552 Therefore, the shape factor must be a function of both $\langle c \rangle$ and w_s . In the limit of van-
 553 ishing density stratification, the shape factor \mathcal{S} must approach the shape factor of the

554 Rouse profile, $\mathcal{S}_{\mathcal{R}}$, which is independent of $\langle c \rangle$, or \mathcal{M} . As stratification strengthens, the
 555 shape factor must reflect the effect of density stratification. To this end, we impose the
 556 following functional form for \mathcal{S} :

$$\mathcal{S}(\mathcal{R}, \mathcal{M}) = \mathcal{S}_{\mathcal{R}}(\mathcal{R}) f(\mathcal{R}, \mathcal{M}), \quad (33)$$

557 where f quantifies the amplification of \mathcal{S} due to density stratification. In the limit
 558 of vanishing density stratification, f must approach unity to ensure the concentration
 559 profile is Rousean. When density stratification strengthens, f must increase. The given
 560 mathematical form in Equation 33 requires the quantification of $\mathcal{S}_{\mathcal{R}}$ and f . To deter-
 561 mine $\mathcal{S}_{\mathcal{R}}$ the Rouse profile was integrated by approximating it as a series sum, which is
 562 discussed in Appendix A in detail. The resultant shape factor reads

$$\mathcal{S}_{\mathcal{R}} = \left(\frac{h - z_o}{z_o} \right)^{\mathcal{R}} \left(\frac{\mathcal{R}^2 - 3\mathcal{R} + 2}{\mathcal{R}^2 - 2\mathcal{R} + 2} \right) \quad (34)$$

563 One can infer from the above equation that when $\mathcal{R} \rightarrow 0$, the shape factor recov-
 564 ers to 1, which is the shape factor for uniform sediment concentration. Increasing Rouse
 565 number will increase the shape factor mainly because of the first multiplicative term in
 566 parenthesis on the right-hand side of Equation 34. For discussion on the accuracy of the
 567 second-order approximation, the reader is referred to Appendix A.

568 Similarly, the shape factor of the modified Rouse profile in the following equation
 569 is obtained after integrating the modified Rouse profile by approximating the concen-
 570 tration profile as a series sum (see Appendix B for detailed derivation):

$$\mathcal{S} = \left(\frac{h}{h - z_o} \right)^{\mathcal{R}\mathcal{M}} \left[\frac{\mathcal{R}^2 - 3\mathcal{R} + 2}{(\mathcal{M} + 1)\mathcal{R}^2 - (\mathcal{M} + 2)\mathcal{R} + 2} \right]. \quad (35)$$

571 The ratio between the shape factors of the modified and non-modified Rouse pro-
 572 files, that is, $S/S_{\mathcal{R}}$, finds f after straightforward algebraic steps:

$$f(\mathcal{R}, \mathcal{M}) = \left(\frac{h}{h - z_o} \right)^{-\mathcal{R}\mathcal{M}} \left(1 - \mathcal{M} \frac{\mathcal{R}^2 - \mathcal{R}}{\mathcal{R}^2 - 2\mathcal{R} + 2} \right)^{-1}. \quad (36)$$

573 The reference height can be considered negligibly small relative to the flow depth,
 574 so that $h - z_o \approx h$, making the first multiplicative term on the right-hand side one.

575 With this simplification, Equation 36 is further reduced to

$$f(\mathcal{R}, \mathcal{M}) = \left(1 - \mathcal{M} \frac{\mathcal{R}^2 - \mathcal{R}}{\mathcal{R}^2 - 2\mathcal{R} + 2} \right)^{-1}. \quad (37)$$

576 In the low settling velocity limit, the second term within the parenthesis approaches
 577 zero, that is

$$\mathcal{M} \frac{\mathcal{R}^2 - \mathcal{R}}{\mathcal{R}^2 - 2\mathcal{R} + 2} \rightarrow 0. \quad (38)$$

578 In this limit, $f(\mathcal{R}, \mathcal{M})$ can be approximated to

$$f(\mathcal{R}, \mathcal{M}) = 1 + \mathcal{M} \frac{\mathcal{R}^2 - \mathcal{R}}{\mathcal{R}^2 - 2\mathcal{R} + 2}. \quad (39)$$

579 Referring to the definition of \mathcal{M} (see Equation 17) and after a few algebraic steps,
 580 we obtained the following as the shape factor

$$S = S_{\mathcal{R}} + \mathcal{G}(\mathcal{R})\langle c \rangle, \quad (40)$$

581 where

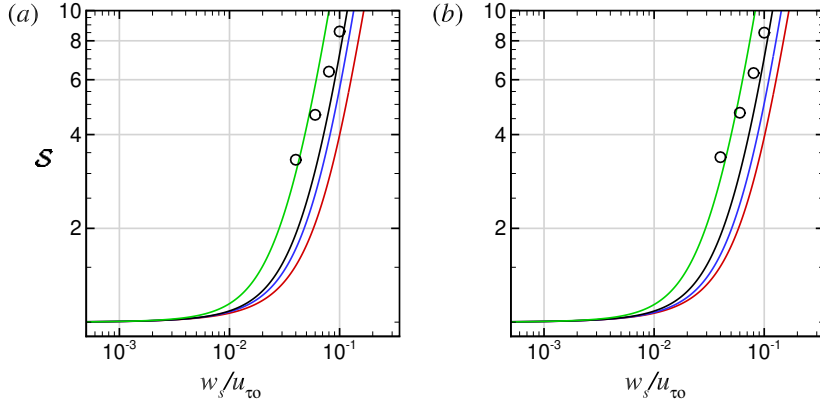


Figure 6: Comparison of the shape factors obtained from the simulations (hollow circles) and those obtained from Equation 40 (solid curves) for (a) $\sin \theta = 0.005$ and (b) $\sin \theta = 0.005$. Curves in red, blue, black, and green in both panels are obtained by using the respective values of S_c and \mathcal{M} from A1-5 and B1-5.

$$\mathcal{G}(\mathcal{R}) = \left[\frac{\alpha(s-1)gh}{u_{\tau o}^2} \right] \mathcal{R}^2 \mathcal{S}_{\mathcal{R}}. \quad (41)$$

582 The shape factor obtained from Equation 40 is compared with those obtained from
 583 the simulations in Figure 6. We used the depth-averaged concentration to obtain the Monin-
 584 Obukhov parameter in the simulations. Equations 40 and 41 estimate the shape factor
 585 of the simulated cases, suggesting that the assumption to obtain the shape factor are rea-
 586 sonable and can be faithfully used. Referring to Equation 22 and the definition of the
 587 densimetric Froude number (see Equation 25), one can obtain the deposition flux as fol-
 588 lows

$$\left(\frac{w_s}{u_{\tau o}} \right) \mathcal{S}\langle c \rangle = (\kappa S_c \mathcal{R}) \mathcal{S}_{\mathcal{R}} \left[\langle c \rangle + \alpha \left(\frac{\mathcal{R}}{Fr_o} \right)^2 \langle c \rangle^2 \right]. \quad (42)$$

589 From the quadratic dependence of settling flux on depth-averaged sediment con-
 590 centration, the nonlinearity in the settling flux induced by density stratification can clearly
 591 be inferred. With the settling and erosion fluxes at hand, the depth-integrated dynamic
 592 equation of sediment concentration becomes

$$\frac{1}{u_{\tau o}} \frac{d\langle c \rangle h}{dt} = \left(\frac{m_e}{u_{\tau o}} \right) \xi - (\kappa S_c \mathcal{R}) \mathcal{S}_{\mathcal{R}} \langle c \rangle + \left[\left(\frac{m_e}{u_{\tau o}} \right) \left(\frac{1 + \xi}{2} \right) \left(\frac{\sin \theta}{Fr_o^2} \right)^2 - (\alpha \kappa S_c) \left(\frac{\mathcal{R}^3 \mathcal{S}_{\mathcal{R}}}{Fr_o^2} \right) \right] \langle c \rangle^2. \quad (43)$$

593 The rightmost term in Equation 43 accounts for the nonlinear effects of density strat-
 594 ification and the cross-shelf gravity force as an explicit function of the depth-integrated
 595 concentration $\langle c \rangle$. The implications of Equation 43 will be discussed in the following sub-
 596 section.

597 4.3 Applications

598 From the dynamic depth-integrated sediment concentration equation, one can in-
 599 fer that the right-hand side of Equation 43 must have real root(s) for equilibrium to es-
 600 tablish. When the coefficient in front of the second-order term on the right-hand side
 601 is positive and there is no sediment suspension initially, the growth in sediment suspen-
 602 sion will cease when $\langle c \rangle$ reaches the smaller root (see Figure 7a for graphical description).
 603 If the coefficient in front of the second-order term on the right-hand side of Equation 43
 604 is negative, equilibrium will be established around the only positive root (see Figure 7b).
 605 Note that the lower root is inherently negative in the latter case. Around the equilib-
 606 rium concentration, any small change in concentration will be forced to return back to
 607 the equilibrium concentration.

608 Equation 43 allows us to determine the parametric relation that marks the tran-
 609 sition of ACSTCs to self-driven turbidity currents. In addition, the depth-averaged con-
 610 centration of ACSTCs under equilibrium conditions can also be determined by using Equa-
 611 tion 43. In the following two subsections, we will respectively discuss the relations for
 612 stability and suspended sediment load.

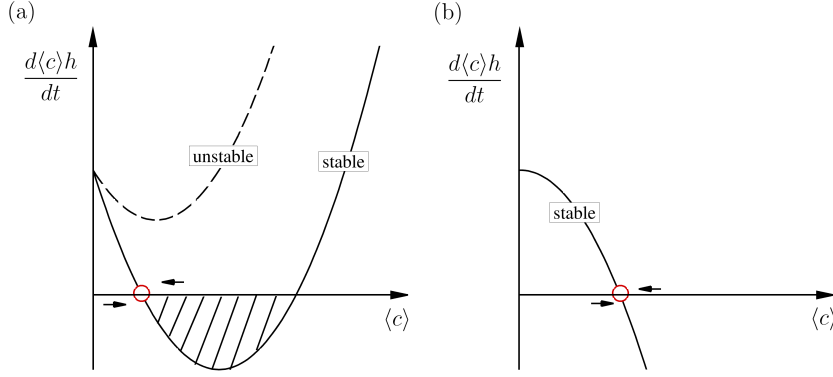


Figure 7: Descriptive sketch for the stability of the dynamic depth-integrated concentration equation for (a) $\alpha\kappa \left(\frac{\mathcal{R}^2 \mathcal{F}(\mathcal{R})}{Fr_o^2} \right) > \left(\frac{m_e}{u_{\tau o}} \right) \left(\frac{1 + \xi}{2} \right) \left(\frac{\sin \theta}{Fr_o^2} \right)^2$ (b) $\alpha\kappa \left(\frac{\mathcal{R}^2 \mathcal{F}(\mathcal{R})}{Fr_o^2} \right) < \left(\frac{m_e}{u_{\tau o}} \right) \left(\frac{1 + \xi}{2} \right) \left(\frac{\sin \theta}{Fr_o^2} \right)^2$. Condition in (a) makes the right-hand side of Equation 43 a convex curve, which may or may not have a real root. The condition in (b) makes the flow stable because the right-hand side of Equation 43 is a concave curve, which has a positive root.

613 4.3.1 Stability Conditions for ACSTCs and Turbidity Current Trigger

614 For the right-hand side of Equation 43 to have real roots, its discriminant must be
 615 positive, which leads to the following inequality after straightforward algebraic steps

$$(\kappa S_c \mathcal{R} S_{\mathcal{R}})^2 + 4\alpha\kappa S_c \xi \left(\frac{m_e}{u_{\tau o}} \right) \frac{\mathcal{R}^3 S_{\mathcal{R}}}{Fr_o^2} > 2\xi(1 + \xi) \left(\frac{m_e}{u_{\tau o}} \right)^2 \left(\frac{\sin \theta}{Fr_o^2} \right)^2. \quad (44)$$

616 For a better physical interpretation, Equation 44 is divided by $(w_s/u_{\tau o})^2$, or $(\kappa S_c \mathcal{R})^2$,
 617 which reads

$$\underbrace{\mathcal{S}_{\mathcal{R}}^2}_I + 4\alpha\xi \underbrace{\left(\frac{m_e}{w_s} \right) \frac{\mathcal{R}^2 S_{\mathcal{R}}}{Fr_o^2}}_{II} > \underbrace{2\xi(1 + \xi) \left(\frac{m_e}{w_s} \right)^2 \left(\frac{\sin \theta}{Fr_o^2} \right)^2}_{III} \quad (45)$$

618 Equation 45 has three terms, denoted as I, II, and III, which are associated with
 619 different physical mechanisms. The first term solely depends on the Rouse profile's shape
 620 factor, that is $\mathcal{S}_{\mathcal{R}}$. Because increasing sediment size or w_s reduces sediment suspension

621 in a Rousean profile, term I can be considered as resistance to suspension due to a stronger
 622 settling effect. With increasing w_s sediments tend to deposit, creating a favorable con-
 623 dition for stability. It must be noted that this term is dissociated from density strati-
 624 fication because it would be present even in the absence of density stratification. Dis-
 625 sociation of term I from density stratification can be inferred from its dependence on the
 626 shape factor of the Rouse profile because the Rouse profile does not consider any tur-
 627 bulence dissipation due to density stratification.

628 The second term, that is term II, is associated with the stabilizing effect of den-
 629 sity stratification. Although it has a stabilizing effect on ACSTCs, this term includes m_e
 630 and ξ , which govern the entrainment from the bed, which also creates a higher downs-
 631 lope gravity force. This may appear counter-intuitive at first, but the following offers an
 632 explanation. The amount of sediments entrained, which is quantified through $m_e\xi$, will
 633 enhance the density stratification -quantified by the product of $m_e\xi$ and Fr_o^{-2} - changes
 634 the shape of the concentration profile through $\alpha\mathcal{R}^3\mathcal{S}_{\mathcal{R}}Fr_o^{-2}$, and thus resist suspension.
 635 Finally, the third term mathematically describes the potential of entrainment growth due
 636 to cross-shelf gravity force.

637 The stability condition in Equation 45 is compared with the simulation results. In
 638 the numerical simulations, w_s and $\sin\theta$ were varied while the other terms were kept con-
 639 stant. Therefore, we plot I+II-III against $w_s/u_{\tau o}$ in Figure 7, where its intercept locates
 640 the critical settling velocity for (in)stability. The critical settling velocity is found as $w_s/u_{\tau o} =$
 641 0.024 for $\sin\theta = 0.01$. The critical settling velocity falls between $w_s/u_{\tau o} = 0.02$ and
 642 $w_s/u_{\tau o} = 0.04$, which are respectively the unstable and stable cases in the simulations
 643 conducted for $\sin\theta = 0.01$. Albeit limited in number, the simulations support Equa-
 644 tion 45's capability to delineate the stable and unstable conditions for ACSTCs.

645 The magnitudes of each term provide information as to the dominant mechanisms
 646 that (de)stabilize ACSTCs. To this end, Figure 9 plots the absolute values of terms I,
 647 II, and III against $w_s/u_{\tau o}$. From figure 9, one can observe that especially when $w_s/u_{\tau o} \rightarrow$

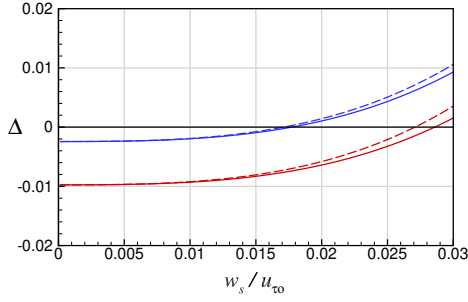


Figure 8: Variation of $\Delta = \text{I} + \text{II} - \text{III}$ with respect to w_s/u_{τ_o} . Curves in blue and red respectively indicate $\sin \theta = 0.005$ and $\sin \theta = 0.01$. Solid and dashed curves indicate the minimum and the maximum values of Δ from different α and S_c combinations listed in Table 2

648 0, term III becomes dominant and results in instability. In this limit, the magnitude of
 649 terms I and II are substantially lower than that of term III (see Figure 9a), and the mag-
 650 nitude of term I is larger than that of term II for $w_s/u_{\tau_o} < 0.002$ (see Figure 3b). How-
 651 ever, the growth rate of term II with respect to w_s/u_{τ_o} is significantly larger than that
 652 of term I, and its magnitude becomes an order of term I's magnitude, suggesting that
 653 density stratification becomes the dominant mechanism to maintaining ACSTCs, espe-
 654 cially for $w_s/u_{\tau_o} > 0.01$. It is worth reiterating that density stratification is a function
 655 of the entrainment parameters because the amount of entrained sediments controls the
 656 amount of sediment suspension, and the amount of sediment suspension governs the den-
 657 sity stratification. Referring to the gradient Richardson number profiles, one should note
 658 that the dominant role of sediment-induced density stratification does not warrant a crit-
 659 ically stratified condition. Density stratification may impose control on the sediment sus-
 660 pension even under subsaturated conditions.

661 **4.3.2 Estimation of Depth-averaged Sediment Concentration**

662 For the specified problem herein, in which there is no initial sediment suspension,
 663 depth-averaged concentration will equilibrate at the smaller root of Equation 43's right-
 664 hand side. Equilibrium concentration will therefore read

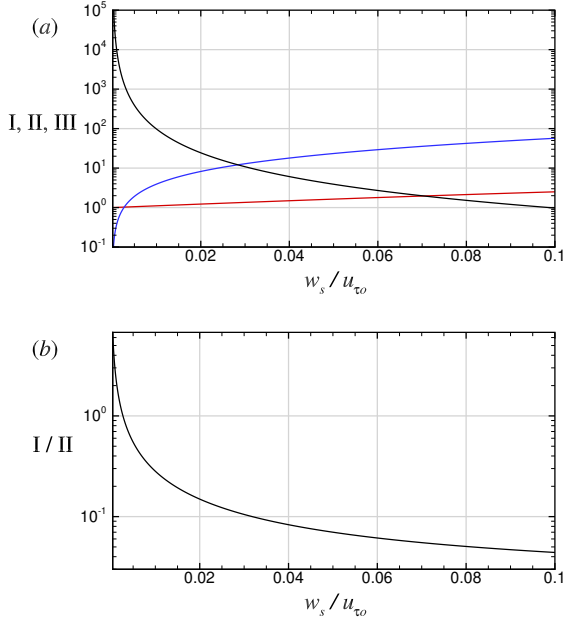


Figure 9: (a) Magnitude of terms I, II, and III for Case A4. Note that Terms I and II are independent of $\sin \theta$ while III is linearly proportional to $\sin \theta$. (b) Variation of the ratio between the destabilizing terms due to settling and density stratification that is I/II, with respect to w_s/u_{τ_o} . Note in both subfigures that ξ , m_e , and Fr_o are taken as constants.

$$\langle c \rangle = \frac{Fr_o^2 - \sqrt{Fr_o^4 - 2\xi(1+\xi) \left(\frac{m_e}{\mathcal{S}_{\mathcal{R}} w_s} \sin \theta \right)^2 + 4\alpha\xi \left(\frac{m_e}{\mathcal{S}_{\mathcal{R}} w_s} \right) (\mathcal{R} Fr_o)^2}}{(1+\xi) \left(\frac{m_e}{\mathcal{S}_{\mathcal{R}} w_s} \right) \left(\frac{\sin \theta}{Fr_o} \right)^2 - 2\alpha\mathcal{R}^2}. \quad (46)$$

665 Depth-averaged concentration estimate from Equation 46 is plotted in Figure 10
 666 with respect to w_s/u_{τ_o} and compared with the amount of sediment suspension obtained
 667 from the simulations. The solid and the dashed curves plotted in the same figure respec-
 668 tively indicate the depth-averaged sediment concentration obtained by using the S_c and
 669 \mathcal{M} combinations that gives the smallest and the largest sediment concentration. There
 670 is a close match between the sediment suspension amount estimated by Equation 46 and
 671 those obtained from the simulations. Noting that the depth-averaged sediment concen-
 672 tration depends on entrainment parameters, sediment settling velocity (or the Rouse num-
 673 ber), cross-shelf bed gradient, and α , the amount of sediment suspension cannot simply
 674 be estimated by a critical Richardson number. This is true even though the amount of

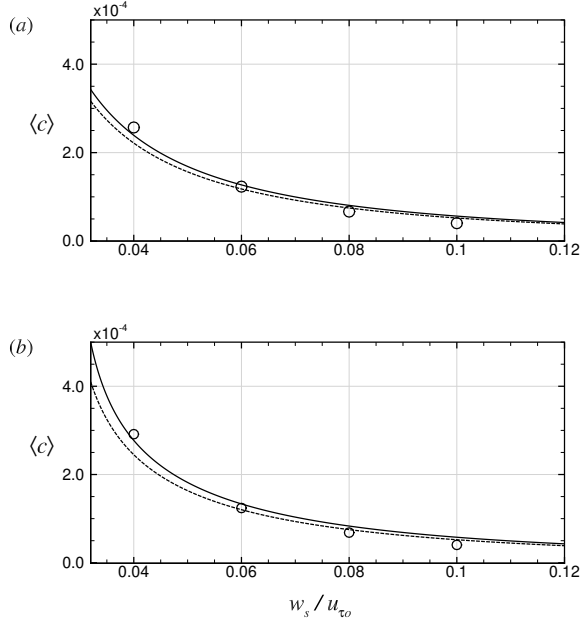


Figure 10: Comparison between the estimated (Equation 46) and observed (hollow circles) volumetric suspended sediment concentration from the simulations for (a) $\sin \theta = 0.005$ and (b) $\sin \theta = 0.01$. Solid and dashed curves indicate the maximum and the minimum concentration obtained from different α and S_c combinations listed in Table 2.

675 suspension in ACSTCs is controlled by density stratification, which can be inferred from
 676 the stability condition in Equation 45 in that density stratification is controlled by both
 677 the settling velocity and the amount of suspension. And the amount of sediment sus-
 678 pension is governed by the erosion parameters along with the settling velocity and the
 679 strength of the bed shear stress. On the other hand, the bulk Richardson number con-
 680 sideres only the amount of sediment suspension, the velocity of the alongshelf current, and
 681 the cross-shelf velocity of ACSTCs.

682 5 Conclusions

683 In this study, an analytical dynamic depth-integrated concentration equation was
 684 developed for ACSTCs. The model developed accounts for the non-linearity associated
 685 with the positive feedback loop between the sediment entrainment and the cross-shelf
 686 gravity force, as well as the sediment-induced density stratification. These non-linear mech-

687 anisms are approximated as explicit quadratic functions of depth-averaged suspended
 688 sediment concentration ($\langle c \rangle$). From the model developed, a quantitative relation for the
 689 critical conditions for the trigger of a self-driven turbidity current that grows out of an
 690 ACSTC is developed. It is found that the critical condition for self-driven turbidity cur-
 691 rent trigger depends on the parameters that help grow the amount of sediment suspen-
 692 sion. These parameters include the cross-shelf bed gradient, sediment entrainment pa-
 693 rameters, m_e and ξ , settling velocity, or the shape factor for the Rouse profile (\mathcal{S}_R), and
 694 the parameters associated with sediment-induced density stratification.

695 The two stabilizing terms and one destabilizing term in Equation 45, which finds
 696 the critical conditions for the trigger, provide information regarding the governing phys-
 697 ical processes in ACSTCs. The destabilizing term, namely term III, quantifies the pos-
 698 itive feedback loop between the sediment entrainment and the cross-shelf gravity force
 699 and is a function of the cross-shelf bed slope, ease of entrainment m_e/w_s and normal-
 700 ized excess shear stress due to alongshelf current ξ . The first stabilizing term, that is term
 701 I, is the sediment settling flux, independent of sediment-induced density stratification.
 702 The second stabilizing term quantifies sediment-induced density stratification effect on
 703 the amount of sediment suspension, which is a function of α , sediment settling velocity,
 704 and entrainment parameters, which are sediment entrainment rate m_e and normalized
 705 excess shear stress due to alongshelf current ξ . The magnitude of term II, which quan-
 706 tifies density stratification, relative to that of term I, which quantifies mere settling, is
 707 substantially larger for the most part except when $w_s \rightarrow 0$. In this limit, density strat-
 708 ification almost vanishes, making the mere settling term the only stabilizing mechanism.
 709 However, with increasing $w_s/u_{\tau o}$, term II sharply increases and outgrows term I. There-
 710 fore, it is concluded that density stratification is the dominant mechanism to maintain
 711 ACSTCs.

712 The amount of depth-averaged sediment concentration found in Equation 46 is a
 713 function of settling velocity, excess shear stress, and sediment entrainment parameters.

714 This finding suggests that the depth-averaged concentration is governed by the balance
 715 of sediment entrainment, density stratification, and mere settling. Bulk Richardson num-
 716 ber showed a five-fold change in the simulations without reaching a global constant value.
 717 Furthermore, in all the simulated ACSTCs, the gradient Richardson number profiles do
 718 not collapse onto a single curve, suggesting that critical density stratification does not
 719 regulate sediment entrainment and deposition, and critical density stratification is not
 720 a necessary condition for ACSTCs. All the findings suggest that depth-integrated suspended
 721 sediment concentration and the critical conditions for the turbidity current generation
 722 out of ACSTCs are regulated by the density stratification, sediment entrainment, includ-
 723 ing its nonlinear interaction with the downslope gravity force, and deposition. All these
 724 findings provide evidence to our hypotheses in Section 1.3.

725 **Appendix A Derivation of the Rouse Profile's Shape Factor**

726 The shape factor for the Rouse profile $\mathcal{S}_{\mathcal{R}}$ is the ratio between the sediment con-
 727 centration at the bed and the depth-averaged concentration. To integrate the Rouse pro-
 728 file conveniently, it will be expressed in dimensionless form, where the distance from the
 729 bed is normalized by the depth, that is $\tilde{z} = z/h$. The dimensionless Rouse profile reads

$$c = c_o \left(\frac{\tilde{z}_o}{1 - \tilde{z}_o} \right)^{\mathcal{R}} \tilde{z}^{-\mathcal{R}} (1 - \tilde{z})^{\mathcal{R}}, \quad (\text{A1})$$

730 where $\tilde{z}_o = z_o/h$. The integration of the dimensionless Rouse profile yields the
 731 depth-averaged concentration $\langle c \rangle$

$$\int_{\tilde{z}=\tilde{z}_o}^{\tilde{z}=1} c(\tilde{z}) d\tilde{z} = h^{-1} \int_{z=z_o}^{z=h} c(z) dz \quad (\text{A2})$$

732 because $dz = h d\tilde{z}$. To analytically obtain the shape factor, $(1 - \tilde{z})^{\mathcal{R}}$ is expanded
 733 as a binomial series

$$(1 - \tilde{z})^{\mathcal{R}} = 1 - \mathcal{R}\tilde{z} + \mathcal{R}(\mathcal{R} - 1)\frac{\tilde{z}^2}{2} - \mathcal{R}(\mathcal{R} - 1)(\mathcal{R} - 2)\frac{\tilde{z}^3}{6} + \dots \quad (\text{A3})$$

734 Thus,

$$\tilde{z}^{-\mathcal{R}}(1 - \tilde{z})^{\mathcal{R}} = \tilde{z}^{-\mathcal{R}} - \mathcal{R}\tilde{z}^{1-\mathcal{R}} + \mathcal{R}(\mathcal{R} - 1)\frac{\tilde{z}^{2-\mathcal{R}}}{2} - \mathcal{R}(\mathcal{R} - 1)(\mathcal{R} - 2)\frac{\tilde{z}^{3-\mathcal{R}}}{6} + \dots \quad (\text{A4})$$

735 By utilizing Equation A4, the Rouse profile can be written as

$$c(\tilde{z}) = c_o \left(\frac{\tilde{z}_o}{1 - \tilde{z}_o} \right)^{\mathcal{R}} \left[\tilde{z}^{-\mathcal{R}} - \mathcal{R}\tilde{z}^{1-\mathcal{R}} + \mathcal{R}(\mathcal{R} - 1)\frac{\tilde{z}^{2-\mathcal{R}}}{2} - \mathcal{R}(\mathcal{R} - 1)(\mathcal{R} - 2)\frac{\tilde{z}^{3-\mathcal{R}}}{6} + \dots \right] \quad (\text{A5})$$

736 First-, second-, and third-order approximations are compared with the actual Rouse
 737 profiles for $w_s/u_{\tau o} = 0.04$ and 0.10 in Figure A1. Past the first order, approximated
 738 concentration profiles are close to one another. For the settling velocities selected, se-
 739 rial approximation follows the actual Rouse profile. The error mainly occurs close to the
 740 top boundary where there is a sharp concentration gradient. Integration of Equation A5
 741 will result in

$$\int c(\tilde{z})d\tilde{z} = c_o \left(\frac{\tilde{z}_o}{1 - \tilde{z}_o} \right)^{\mathcal{R}} \left[\frac{1}{1 - \mathcal{R}}\tilde{z}^{1-\mathcal{R}} - \frac{\mathcal{R}}{2 - \mathcal{R}}\tilde{z}^{2-\mathcal{R}} + \frac{\mathcal{R}(\mathcal{R} - 1)}{2(3 - \mathcal{R})}\tilde{z}^{3-\mathcal{R}} - \dots \right] + \mathcal{A} \quad (\text{A6})$$

742 where \mathcal{A} is the constant of integration. Since $z_o/h = \tilde{z} \approx 0$, the lower bound of
 743 the integral can be neglected. Approximating the term within the brackets up to the second-
 744 order, that is $\mathcal{O}(\tilde{z}^2)$, the integral of the Rouse profile is obtained as

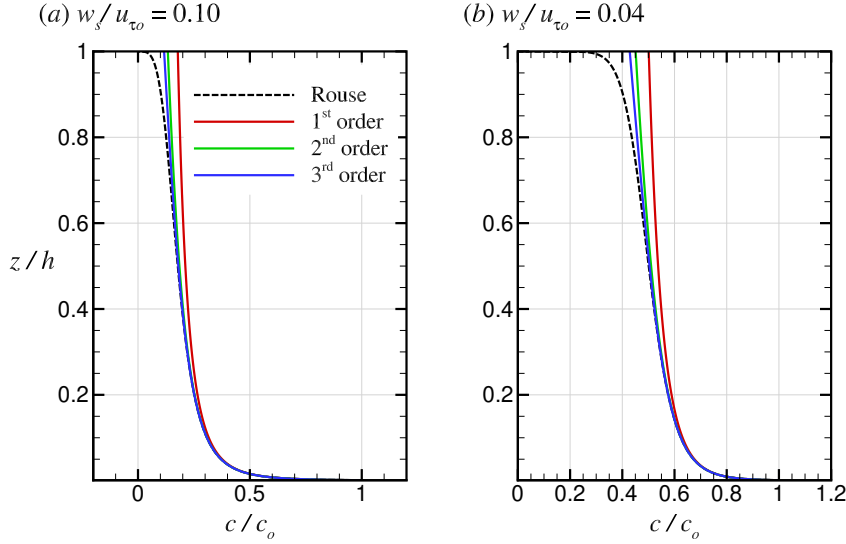


Figure A1: Comparison of the first- (red), second- (green), and third-order (blue) approximations of the Rouse profile with the actual Rouse profile (dashed curve) for (a) $w_s/u_{\tau_o} = 0.10$ and (b) $w_s/u_{\tau_o} = 0.04$. Note that the concentration profiles are normalized by the reference concentration c_o and becomes unity at the reference height z_o .

$$\int_{\tilde{z}=\tilde{z}_o}^{\tilde{z}=1} c(\tilde{z})d\tilde{z} = c_o \left(\frac{\tilde{z}_o}{1-\tilde{z}_o} \right)^{\mathcal{R}} \left(\frac{\mathcal{R}^2 - 2\mathcal{R} + 2}{\mathcal{R}^2 - 3\mathcal{R} + 2} \right) \quad (\text{A7})$$

745 By approximating the sediment concentration at the bed to the reference concen-
 746 tration, that is $c_b \approx c_o$, the shape factor for the Rouse profile will be obtained as

$$\mathcal{S}_{\mathcal{R}} = \frac{c_o}{\int_{\tilde{z}=\tilde{z}_o}^{\tilde{z}=1} c(\tilde{z})d\tilde{z}} = \left(\frac{h-z_o}{z_o} \right)^{\mathcal{R}} \left(\frac{\mathcal{R}^2 - 3\mathcal{R} + 2}{\mathcal{R}^2 - 2\mathcal{R} + 2} \right) \quad (\text{A8})$$

747 Appendix B Derivation of the Modified Rouse Profile's Shape Fac- 748 tor

749 The shape factor for the modified Rouse profile \mathcal{S} is determined similar to that for
 750 the Rouse profile. The dimensionless modified Rouse profile reads

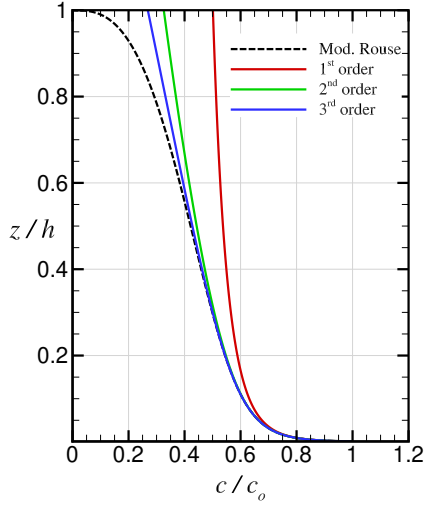


Figure B1: Comparison of the first- (red), second- (green), and third-order (blue) approximations of the modified Rouse profile with the actual modified Rouse profile (dashed curve) for $w_s/u_{\tau_o} = 0.04$. The Monin-Obukhov parameter $\mathcal{M} = 25$. Various values of \mathcal{M} are also tested and similar results are obtained; therefore, only the profiles from $\mathcal{M} = 25$ is shown for brevity. Note that the concentration profiles are normalized by the reference concentration c_o and becomes unity at the reference height z_o .

$$c = c_o \left[\frac{\tilde{z}_o^{\mathcal{R}}}{(1 - \tilde{z}_o)^{\mathcal{R}(\mathcal{M}+1)}} \right] \tilde{z}^{-\mathcal{R}} (1 - \tilde{z})^{\mathcal{R}(\mathcal{M}+1)} \quad (\text{B1})$$

751 After expanding $(1 - \tilde{z})^{\mathcal{R}(\mathcal{M}+1)}$ as binomial series similar to that for the Rouse pro-
 752 file, $\tilde{z}^{-\mathcal{R}} (1 - \tilde{z})^{\mathcal{R}(\mathcal{M}+1)}$ is obtained as

$$\begin{aligned} \tilde{z}^{-\mathcal{R}} (1 - \tilde{z})^{\mathcal{R}(\mathcal{M}+1)} = & \tilde{z}^{-\mathcal{R}} - (\mathcal{R}\mathcal{M} + \mathcal{R})\tilde{z}^{1-\mathcal{R}} + (\mathcal{R}\mathcal{M} + \mathcal{R} - 1)(\mathcal{R}\mathcal{M} + \mathcal{R})\frac{\tilde{z}^{2-\mathcal{R}}}{2} \\ & - (\mathcal{R}\mathcal{M} + \mathcal{R} - 2)(\mathcal{R}\mathcal{M} + \mathcal{R} - 1)(\mathcal{R}\mathcal{M} + \mathcal{R})\frac{\tilde{z}^{3-\mathcal{R}}}{6} + \dots \end{aligned} \quad (\text{B2})$$

753 Using Equation B2, the modified Rouse profile is then obtained as

$$c(\tilde{z}) = c_o \frac{\tilde{z}_o^{\mathcal{R}}}{(1 - \tilde{z}_o)^{\mathcal{R}(\mathcal{M}+1)}} \left[\tilde{z}^{-\mathcal{R}} - (\mathcal{R}\mathcal{M} + \mathcal{R})\tilde{z}^{1-\mathcal{R}} + (\mathcal{R}\mathcal{M} + \mathcal{R} - 1)(\mathcal{R}\mathcal{M} + \mathcal{R})\frac{\tilde{z}^{2-\mathcal{R}}}{2} - \dots \right] \quad (\text{B3})$$

754 Approximated concentration profiles are shown for the first, second, and the third
 755 orders in Figure B1. From the same figure, one can observe that increasing order of ap-
 756 proximation improves the accuracy, but the difference between the second- and the third-
 757 order approximations is small. Therefore, we will use the second-order approximation
 758 henceforth. For the second-order approximation, the integral of the concentration pro-
 759 file becomes

$$\int c(\tilde{z})d\tilde{z} = c_o \frac{\tilde{z}_o^{\mathcal{R}}}{(1 - \tilde{z}_o)^{\mathcal{R}\mathcal{M}}} \tilde{z}^{-\mathcal{R}} \left[\frac{1}{1 - \mathcal{R}} \tilde{z} - \frac{\mathcal{R}\mathcal{M} + \mathcal{R}}{2 - \mathcal{R}} \tilde{z}^2 + \frac{(\mathcal{R}\mathcal{M} + \mathcal{R})(\mathcal{R}\mathcal{M} + \mathcal{R} - 1)}{2(3 - \mathcal{R})} \tilde{z}^3 - \dots \right] + \mathcal{B} \quad (\text{B4})$$

760 where \mathcal{B} is the constant of integration. Since $z_o/h \approx 0$, the lower bound of the
 761 integral can be neglected. Keeping the terms up to the second-order, that is $\mathcal{O}(\tilde{z}^2)$, the
 762 integral of the Rouse profile is obtained as

$$\int_{\tilde{z}=\tilde{z}_o}^{\tilde{z}=1} c(\tilde{z})d\tilde{z} = c_o \frac{\tilde{z}_o^{\mathcal{R}}}{(1 - \tilde{z}_o)^{\mathcal{R}\mathcal{M}+\mathcal{R}}} \left[\frac{(\mathcal{M} + 1)\mathcal{R}^2 - (\mathcal{M} + 2)\mathcal{R} + 2}{\mathcal{R}^2 - 3\mathcal{R} + 2} \right] \quad (\text{B5})$$

763 From the depth-averaged concentration, the shape factor for the modified Rouse
 764 profile will be obtained as

$$\mathcal{S} = \frac{c_o}{\int_{\tilde{z}=\tilde{z}_o}^{\tilde{z}=1} c(\tilde{z})d\tilde{z}} = \left(\frac{z_o}{h - z_o} \right)^{\mathcal{R}} \left(\frac{h}{h - z_o} \right)^{\mathcal{R}\mathcal{M}} \left[\frac{\mathcal{R}^2 - 3\mathcal{R} + 2}{(\mathcal{M} + 1)\mathcal{R}^2 - (\mathcal{M} + 2)\mathcal{R} + 2} \right] \quad (\text{B6})$$

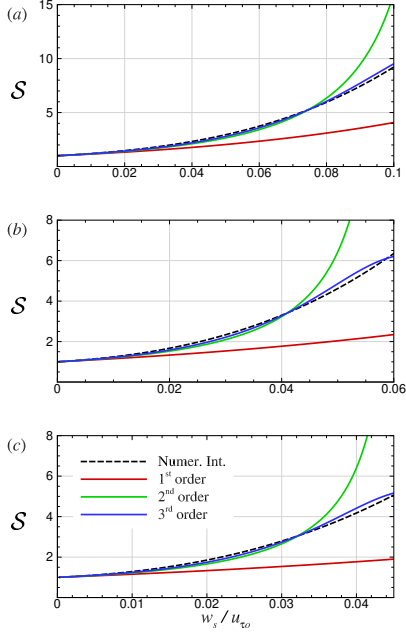


Figure B2: Comparison of the the modified Rouse profile's first, second, and third-order approximations with those obtained from the numerical integration of the modified Rouse profile. The Monin-Obukhov paramater is $\mathcal{M} = 25$ in (a), $\mathcal{M} = 90$ in (b), and $\mathcal{M} = 150$ in (c).

765 The shape factor obtained is also compared with its first- and third-order order coun-
766 terpart as well as the shape factor obtained after numerically integrating the modified
767 Rouse profile (see Figure B2). The second- and the third-order approximations are close
768 to the numerically integrated shape factor from $w_s/u_{\tau_o} = 0$ to $w_s/u_{\tau_o} = 0.80$, $w_s/u_{\tau_o} =$
769 0.45, and $w_s/u_{\tau_o} = 0.34$ for $\mathcal{M} = 25$, $\mathcal{M} = 90$, and $\mathcal{M} = 150$, respectively. There-
770 fore, the settling velocity range where second-order approximation holds narrows with
771 increasing \mathcal{M} . This is also true for the third-order approximation, but the range of ap-
772 plicability for the third-order approximation is slightly larger than the second-order ap-
773 proximation. However, it must be noted that the given analysis is conducted for *a pri-*
774 *ori* \mathcal{M} value. On the other hand, the suspended sediment load, hence the Monin-Obukhov
775 parameter \mathcal{M} , decreases with increasing settling velocity where sediments are sourced
776 from the bed. As such, second- and third-order approximations still remain applicable
777 for increasing settling velocity.

Data Availability

The source code and case setup to reproduce the results and the mean quantities that produced the figures are publicly available in open science framework at <https://doi.org/10.17605/OSF.IO/8BKXR>.

Acknowledgments

Funding for this study was provided by NSF (OCE-20203676). High-performance computational resources provided by Louisiana State University (<http://www.hpc.lsu.edu>) are greatly acknowledged. The majority of the simulations for this study were conducted as a part of the course entitled “High-performance Computing Applications in Environmental Flows” offered by the first author. Ms. Sahar Haddadian is acknowledged for conducting the preliminary simulations, whose results inspired this study.

References

- Ayranci, K., Lintern, D. G., Hill, P. R., & Dashtgard, S. E. (2012). Tide-supported gravity flows on the upper delta front, Fraser River delta, Canada. *Marine Geology*, *326*, 166–170.
- Bhattacharya, J. P., Copeland, P., Lawton, T. F., & Holbrook, J. (2016). Estimation of source area, river paleo-discharge, paleoslope, and sediment budgets of linked deep-time depositional systems and implications for hydrocarbon potential. *Earth-Science Reviews*, *153*, 77–110.
- Cantero, M. I., Balachandar, S., & Garcia, M. H. (2008). An Eulerian–Eulerian model for gravity currents driven by inertial particles. *International Journal of Multiphase Flow*, *34*(5), 484–501.
- Cantero, M. I., Shringarpure, M., & Balachandar, S. (2012). Towards a universal criteria for turbulence suppression in dilute turbidity currents with non-cohesive sediments. *Geophysical Research Letters*, *39*(14).

- 803 Cellino, M., & Graf, W. H. (1999). Sediment-laden flow in open-channels under
804 noncapacity and capacity conditions. *Journal of Hydraulic Engineering*, *125*, 455-
805 462.
- 806 Cheng, Z., Yu, X., Hsu, T.-J., Ozdemir, C. E., & Balachandar, S. (2015). On
807 the transport modes of fine sediment in the wave boundary layer due to resus-
808 pension/deposition: A turbulence-resolving numerical investigation. *Journal of*
809 *Geophysical Research: Oceans*, *120*(3), 1918–1936.
- 810 Chorin, A. J. (1968). Numerical solution of the navier-stokes equations. *Mathematics*
811 *of Computation*, *22*(104), 745–762.
- 812 Cortese, T. A., & Balachandar, S. (1995). High performance spectral simulation
813 of turbulent flows in massively parallel machines with distributed memory. *The*
814 *International Journal of Supercomputer Applications and High Performance Com-*
815 *puting*, *9*(3), 187–204.
- 816 Curran, K., Hill, P., Milligan, T., Mikkelsen, O., Law, B., de Madron, X. D., &
817 Bourrin, F. (2007). Settling velocity, effective density, and mass composition of
818 suspended sediment in a coastal bottom boundary layer, Gulf of Lions, France.
819 *Continental Shelf Research*, *27*(10-11), 1408–1421.
- 820 Denomme, K. C., Bentley, S. J., Harazim, D., & Macquaker, J. H. (2016). Hy-
821 drodynamic controls on muddy sedimentary-fabric development on the Southwest
822 Louisiana subaqueous delta. *Marine Geology*, *382*, 162–175.
- 823 Fain, A., Ogston, A., & Sternberg, R. (2007). Sediment transport event analysis on
824 the western Adriatic continental shelf. *Continental Shelf Research*, *27*(3-4), 431–
825 451.
- 826 Flores, R. P., Rijnsburger, S., Meirelles, S., Horner-Devine, A. R., Souza, A. J.,
827 Pietrzak, J. D., . . . Reniers, A. (2018). Wave generation of gravity-driven sed-
828 iment flows on a predominantly sandy seabed. *Geophysical Research Letters*,
829 *45*(15), 7634–7645.
- 830 Haddadian, S., Ozdemir, C., Goodlow, B., Xue, G., & Bentley, S. (2021). Direct

- 831 numerical simulations of miniature along-shelf current-supported turbidity cur-
832 rents: Conceptual investigation of velocity structure and drag coefficient. *Journal*
833 *of Geophysical Research: Oceans*, 126(8), e2020JC016736.
- 834 Hale, R. P., & Ogston, A. S. (2015). In situ observations of wave-supported fluid-
835 mud generation and deposition on an active continental margin. *Journal of Geo-*
836 *physical Research: Earth Surface*, 120(11), 2357–2373.
- 837 Hooshmand, A., Horner-Devine, A. R., & Lamb, M. P. (2015). Structure of tur-
838 bulence and sediment stratification in wave-supported mud layers. *Journal of Geo-*
839 *physical Research: Oceans*, 120(4), 2430–2448.
- 840 Itakura, T., & Kishi, T. (1980). Open channel flow with suspended sediments. *Jour-*
841 *nal of Hydraulics Division*, 106(8), 1325–1343.
- 842 Jaramillo, S., Sheremet, A., Allison, M., Reed, A., & Holland, K. (2009). Wave-mud
843 interactions over the muddy Atchafalaya subaqueous clinoform, Louisiana, United
844 States: Wave-supported sediment transport. *Journal of Geophysical Research:*
845 *Oceans*, 114(C4).
- 846 Komar, P. D. (1977). Computer simulation of turbidity current flow and the
847 study of deep-sea channels and fan sedimentation. In E. Goldberg, I. McCave,
848 J. O'Brian, & S. J.H. (Eds.), *Marine Modeling (The Sea)* (Vol. 6, p. 603-621).
849 New York: Wiley.
- 850 Ma, Y., Friedrichs, C. T., Harris, C. K., & Wright, L. D. (2010). Deposition by
851 seasonal wave-and current-supported sediment gravity flows interacting with spa-
852 tially varying bathymetry: Waiapu shelf, New Zealand. *Marine Geology*, 275(1-4),
853 199–211.
- 854 Ma, Y., Wright, L. D., & Friedrichs, C. T. (2008). Observations of sediment trans-
855 port on the continental shelf off the mouth of the Waiapu River, New Zealand:
856 Evidence for current-supported gravity flows. *Continental Shelf Research*, 28(4),
857 516-532. doi: <https://doi.org/10.1016/j.csr.2007.11.001>
- 858 Macquaker, J. H., Bentley, S. J., & Bohacs, K. M. (2010). Wave-enhanced sediment-

- 859 gravity flows and mud dispersal across continental shelves: Reappraising sediment
860 transport processes operating in ancient mudstone successions. *Geology*, 38(10),
861 947–950.
- 862 Martin, D., Nittrouer, C., Ogston, A., & Crockett, J. (2008). Tidal and seasonal dy-
863 namics of a muddy inner shelf environment, Gulf of Papua. *Journal of Geophysical*
864 *Research: Earth Surface*, 113(F1).
- 865 Monin, A. S., & Obukhov, A. M. (1954). Basic laws of turbulent mixing in the sur-
866 face layer of the atmosphere. *Contributions to Geophysical Institute of Academy of*
867 *Sciences USSR*, 151(163), e187.
- 868 Ogston, A. S., Sternberg, R. W., Nittrouer, C. A., Martin, D. P., Goñi, M. A., &
869 Crockett, J. S. (2008). Sediment delivery from the Fly River tidally dominated
870 delta to the nearshore marine environment and the impact of El Nino. *Journal of*
871 *Geophysical Research: Earth Surface*, 113(F1).
- 872 Ozdemir, C. E., Hsu, T.-J., & Balachandar, S. (2011). A numerical investigation
873 of lutocline dynamics and saturation of fine sediment in the oscillatory boundary
874 layer. *Journal of Geophysical Research: Oceans*, 116(C9).
- 875 Parker, G., Fukushima, Y., & Pantin, H. M. (1986). Self-accelerating turbidity cur-
876 rents. *Journal of Fluid Mechanics*, 171, 145–181.
- 877 Parsons, J. D., Friedrichs, C. T., Traykovski, P. A., Mohrig, D., Imran, J., Syvitski,
878 J. P., ... others (2007). The mechanics of marine sediment gravity flows. *Con-*
879 *tinental margin sedimentation: from sediment transport to sequence stratigraphy*,
880 37, 275–334.
- 881 Peng, Y., Yu, Q., Du, Z., Wang, L., Wang, Y., & Gao, S. (2022). Gravity-driven sed-
882 iment flows on the shallow sea floor of a muddy open coast. *Marine Geology*, 445,
883 106759.
- 884 Sanford, L. P., & Maa, J. P.-Y. (2001). A unified erosion formulation for fine sedi-
885 ments. *Marine Geology*, 179(1-2), 9–23.
- 886 Sequeiros, O. E., Bolla Pittaluga, M., Frascati, A., Pirmez, C., Masson, D. G.,

- 887 Weaver, P., . . . Rimmer, J. G. (2019). How typhoons trigger turbidity currents in
888 submarine canyons. *Scientific reports*, *9*(1), 1–15.
- 889 Traykovski, P., Geyer, W., Irish, J., & Lynch, J. (2000). The role of wave-induced
890 density-driven fluid mud flows for cross-shelf transport on the eel river continental
891 shelf. *Continental Shelf Research*, *20*(16), 2113–2140.
- 892 Traykovski, P., Trowbridge, J., & Kineke, G. (2015). Mechanisms of surface wave
893 energy dissipation over a high-concentration sediment suspension. *Journal of Geo-*
894 *physical Research: Oceans*, *120*(3), 1638–1681.
- 895 Traykovski, P., Wiberg, P. L., & Geyer, W. R. (2007). Observations and model-
896 ing of wave-supported sediment gravity flows on the Po prodelta and comparison
897 to prior observations from the Eel shelf. *Continental Shelf Research*, *27*(3-4),
898 375–399.
- 899 van Kessel, T., & Kranenburg, C. (1996). Gravity current of fluid mud on sloping
900 bed. *Journal of Hydraulic Engineering*, *122*(12), 710–717.
- 901 Walsh, J. P., Nittrouer, C. A., Palinkas, C. M., Ogston, A. S., Sternberg, R. W., &
902 Brunskill, G. J. (2004). Clinoform mechanics in the Gulf of Papua, New Guinea.
903 *Continental Shelf Research*, *24*(19), 2487–2510.
- 904 Williamson, J. H. (1980). Low-storage Runge-Kutta schemes. *Journal of Computa-*
905 *tional Physics*, *35*(1), 48–56.
- 906 Winterwerp, J. C. (2001). Stratification effects by cohesive and noncohesive sedi-
907 ment. *Journal of Geophysical Research: Oceans*, *106*(C10), 22559–22574.
- 908 Winterwerp, J. C., Lely, M., & He, Q. (2009). Sediment-induced buoyancy destruc-
909 tion and drag reduction in estuaries. *Ocean Dynamics*, *59*(5), 781–791.
- 910 Wright, L., & Friedrichs, C. (2006). Gravity-driven sediment transport on continen-
911 tal shelves: A status report. *Continental Shelf Research*, *26*(17), 2092–2107. doi:
912 <https://doi.org/10.1016/j.csr.2006.07.008>
- 913 Wright, L., Friedrichs, C., Kim, S., & Scully, M. (2001). Effects of ambient cur-
914 rents and waves on gravity-driven sediment transport on continental shelves. *Ma-*

- 915 *rine Geology*, 175(1), 25-45. doi: [https://doi.org/10.1016/S0025-3227\(01\)00140-2](https://doi.org/10.1016/S0025-3227(01)00140-2)
- 916 Yue, L., Cheng, Z., & Hsu, T.-J. (2019). Turbid: A turbulence-resolving numerical
917 model for simulating bottom boundary layer and fine sediment transport.
- 918 Yue, L., Cheng, Z., & Hsu, T.-J. (2020). A turbulence-resolving numerical investi-
919 gation of wave-supported gravity flows. *Journal of Geophysical Research: Oceans*,
920 125(2), e2019JC015220.
- 921 Zang, Z., Xue, Z. G., Xu, K., Ozdemir, C. E., Chen, Q., Bentley, S. J., & Sahin,
922 C. (2020). A numerical investigation of wave-supported gravity flow during
923 cold fronts over the Atchafalaya shelf. *Journal of Geophysical Research: Oceans*,
924 125(9), e2019JC015269.
- 925 Zhang, W., Cui, Y., Santos, A. I., & Hanebuth, T. J. (2016). Storm-driven bottom
926 sediment transport on a high-energy narrow shelf (NW Iberia) and development of
927 mud depocenters. *Journal of Geophysical Research: Oceans*, 121(8), 5751–5772.